

See discussions, stats, and author profiles for this publication at: <https://www.researchgate.net/publication/231661084>

# Test of Trajectory Surface Hopping Against Accurate Quantum Dynamics for an Electronically Nonadiabatic Chemical Reaction

ARTICLE *in* THE JOURNAL OF PHYSICAL CHEMISTRY A · FEBRUARY 1998

Impact Factor: 2.69 · DOI: 10.1021/jp9731922

---

CITATIONS

43

READS

8

## 4 AUTHORS, INCLUDING:



Thomas C Allison

National Institute of Standards and Technolo...

53 PUBLICATIONS 869 CITATIONS

[SEE PROFILE](#)



David W. Schwenke

NASA

256 PUBLICATIONS 7,138 CITATIONS

[SEE PROFILE](#)



Donald Truhlar

University of Minnesota Twin Cities

1,342 PUBLICATIONS 81,158 CITATIONS

[SEE PROFILE](#)

## Test of Trajectory Surface Hopping Against Accurate Quantum Dynamics for an Electronically Nonadiabatic Chemical Reaction

Maria S. Topaler,<sup>†</sup> Thomas C. Allison,<sup>†</sup> David W. Schwenke,<sup>‡</sup> and Donald G. Truhlar\*,<sup>†</sup>

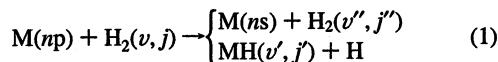
Department of Chemistry and Supercomputer Institute, University of Minnesota,  
Minneapolis, Minnesota 55455-0431, and National Aeronautics Space Administration Ames Research Center,  
Mail Stop 230-3, Moffett Field, California 94035-1000

Received: October 1, 1997; In Final Form: December 19, 1997

This paper presents the first test of the popular trajectory surface-hopping (TSH) method against accurate three-dimensional quantum mechanics for a reactive system. The system considered is a model system in which an excited atom with an excitation energy of 0.76 eV reacts with or is quenched by the H<sub>2</sub> molecule. The electronically nonadiabatic collisions occur primarily near a conical intersection of an exciplex with a repulsive ground state. The accurate quantal results are calculated using the outgoing wave variational principle in an electronically diabatic representation. Four variants of the TSH method are tested, differing in the criteria for hopping and the component of momentum that is adjusted in order to conserve energy when a hop occurs. Coupling between the ground and excited surface occurs primarily in the vicinity of a conical intersection and is mediated by an exciplex found on the upper surface. We find that the overall TSH quenching probabilities are in good agreement with quantum mechanical results, but the branching ratios between reactive and nonreactive trajectories and many of the state-selected results are poorly reproduced by trajectory calculations. The agreement between trajectory surface hopping and quantal results is on average worse for the relatively more “quantum mechanical”  $j = 0$  initial state and M + H<sub>2</sub> quenching process and better for the relatively more “classical”  $j = 2$  initial state and MH + H’ reactive process. We also perform a statistical calculation of overall quenching probability and unimolecular rate of the nonadiabatic decay of the exciplex. We find that only about 10 % of trajectories can be described as “statistical” and that statistical calculation overestimates the total quenching rate significantly.

### 1. Introduction

Trajectory surface hopping<sup>1</sup> (TSH) has become established as the most universally applicable dynamical model for electronically nonadiabatic processes in molecules, and various versions of the basic scheme have been proposed throughout the years. Trajectory surface-hopping methods have been tested against accurate quantum dynamics for an electronically nonadiabatic collision process in full three-dimensional space for one small-gap (fine-structure) problem<sup>2</sup> and one large-gap problem.<sup>3</sup> In the latter case, which is of more interest here, we considered the quenching of Na(3p) by H<sub>2</sub>, and we reported tests of two<sup>4,5</sup> of the most general TSH algorithms. Both methods agreed well with accurate quantum dynamics on the average. In the present paper we report a test of these trajectory surface-hopping algorithms, plus two variants, against accurate quantum dynamics for a three-dimensional reactive collision process. In particular we consider a model system in which nonreactive quenching competes with reaction:



where M denotes a model metal atom with an ns → np excitation energy of 0.76 eV and mass equal to that of Li; H<sub>2</sub> denotes a diatomic molecule with realistic parameters for representing H<sub>2</sub>; v, v', and v'' denote vibrational quantum numbers; and j, j', and j'' denote rotational quantum numbers.

The model system has two coupled electronic states with the same general topology as the widely studied alkali-metal-plus-H<sub>2</sub> systems. The ground diabatic potential energy surface correlates with M(ns) and is purely repulsive, similar to rare-gas-plus-H<sub>2</sub>-potentials. The excited-state diabatic potential energy surface correlates to M(np), with excitation energy 0.76 eV, in the reactant arrangement and to MH(X<sup>1Σ<sup>+</sup></sup>) + H in the product arrangement, which is 0.70 eV endoergic from M(ns) + H<sub>2</sub> and 0.06 eV exoergic from M(np) + H<sub>2</sub>. This surface shows a  $C_{2v}$  minimum (excited-state complex or exciplex) that is bound by about 0.40 eV with respect to the reactant asymptote and by 0.34 eV with respect to the product asymptote. (All these values are potential energies excluding zero-point energies.) The excited-state surface is very flat in the bending degree of freedom, with the minimum-energy configuration as a function of the Jacobi angle  $χ$  (the angle between the H-to-H vector  $\vec{r}$  and the M-to-center-of-mass-of-H<sub>2</sub> vector  $\vec{R}$ ) varying by only a few hundredths of an eV as  $χ$  increases from 0 (collinear) to  $π/2$  ( $C_{2v}$ ). Along a crossing seam that passes near the  $C_{2v}$  exciplex minimum, the excited diabat intersects the ground surface conically for  $C_{2v}$  geometries, with the lowest energy conical intersection 0.39 eV below M(np) + H<sub>2</sub>. As in our previous model of NaH<sub>2</sub>,<sup>6,7</sup> the model system is assumed to have no electronic angular momentum and no momentum coupling<sup>8</sup> between the diabatic electronic states. All other terms in the Hamiltonian for a three-body system are fully included.

Section 2 presents the potential energy surface, section 3 presents the method used for quantum dynamics, and section 4

<sup>†</sup> Department of Chemistry and Supercomputer Institute.  
<sup>‡</sup> NASA Ames Research Center.

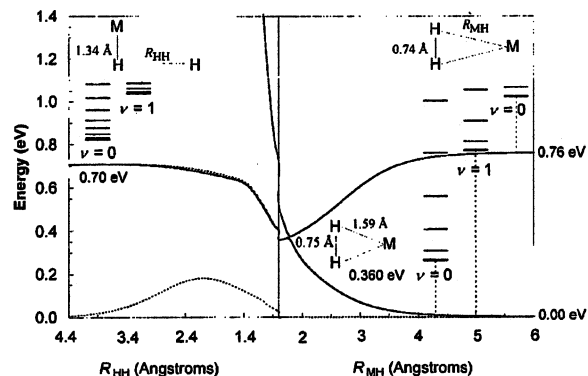


**Figure 1.** Diabatic (dashed lines) and adiabatic (solid lines) potential energy curves along an approximate reaction path (see text). Geometries and several lowest vibrational–rotational energy levels of the ground-state ( $M(ns) + H_2$ ) and the excited-state ( $M(ns) + H_2$ ) reactants, and of the products ( $MH + H$ ) are also shown, as well as the geometry and classical energy of the minimum on the  $U_{22}$  diabatic potential energy surface.

presents the four TSH algorithms to be tested. Section 5 describes the calculations, section 6 discusses the results, and section 7 presents some concluding remarks. Details not needed for understanding the results are presented in supporting information.

## 2. Potential Energy Surfaces

The potential energy surfaces were modeled similarly to our previous two-state model<sup>6</sup> for  $Na + H_2$ . In the diabatic representation of ref 6 the Hamiltonian is equal to

$$H = \frac{\vec{P}_R^2}{2\mu} + \frac{\vec{p}_r^2}{2m} + \begin{pmatrix} U_{11}(R, r, \chi) & U_{12}(R, r, \chi) \\ U_{12}(R, r, \chi) & U_{22}(R, r, \chi) \end{pmatrix} \quad (2)$$

where  $\vec{R}$  and  $\vec{r}$  are the unscaled center-of-mass Jacobi coordinates, and  $\vec{P}_R$  and  $\vec{p}_r$  are their conjugate momenta. The potential energy surfaces depend only on internal coordinates, which are taken to be  $R = |\vec{R}|$ ,  $r = |\vec{r}|$ , and angle  $\chi$  between the  $\vec{R}$  and  $\vec{r}$  vectors. Another choice of internal nuclear coordinates that is used in the discussion consists of the bond coordinates  $R_{HH} = r$  (distance between the two H atoms),  $R_{MH}$ , and  $R_{MH'}$  (distances between the metal atom and each of the hydrogen atoms). In eq 2,  $\mu$  is the reduced mass for the relative motion of M and  $H_2$ ,  $m$  is the reduced mass of  $H_2$ , and 1 denotes a  $2 \times 2$  unit matrix. Adiabatic potential energy surfaces,  $V_1$  and  $V_2$ , are given in terms of the diabatic surfaces as

$$V_{1(2)} = \frac{1}{2}(U_{11} + U_{22}) \mp \sqrt{(U_{22} - U_{11})^2 + 4U_{12}^2} \quad (3)$$

where the minus sign corresponds to the ground-state adiabatic potential energy surface,  $V_1$ , and the plus sign corresponds to the first-excited-state adiabatic potential energy surface,  $V_2$ . The equations defining the surfaces and all their parameters are given in the supporting information. In the rest of this section we describe the critical features of the model system.

Figure 1 shows diabatic and adiabatic potential curves along an approximate reaction path. This reaction path is defined by joining two one-dimensional cuts through the potential energy surfaces: one for  $R_{HH} = R_{HH}^e$  with  $\chi = 90^\circ$  (reactant channel) and another for  $R_{MH} = R_{MH}^e$  with the M–H–H' bond angle equal to  $90^\circ$  (product channel).  $R_{HH}^e$  and  $R_{MH}^e$  are the equilibrium interatomic distances in the corresponding diatomic molecules and are equal to 0.747 and 1.34 Å, respectively. At

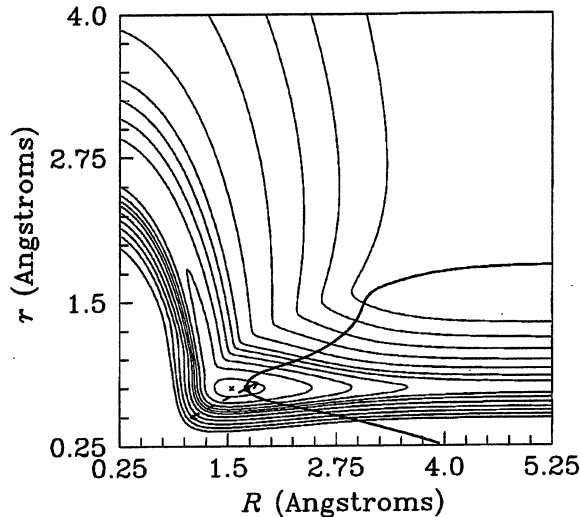


**Figure 2.** Contour plot of the  $U_{22}$  diabatic potential energy surface for  $C_{2v}$  geometries. The seam of conical intersections is shown by a thick solid line, the lowest-energy conical intersection is shown by a solid dot, and the minimum of  $U_{22}$  is shown by a cross. Gradients of the diabatic potential energy surfaces at the minimum-energy conical intersection are shown as solid ( $\nabla U_{11}$ ) and dashed ( $\nabla U_{22}$ ) arrows. (The relative length of the arrows is meaningful, but the absolute length is not.) The contour lines are 0.4, 0.5, 0.6, 0.7, 0.8, 0.9, 1.1, 1.4, 1.8, 2.3, and 2.9 eV.

$C_{2v}$  geometries ( $\chi = 90^\circ$ ) the diabatic coupling is zero by symmetry, so that the adiabatic and diabatic representations are identical, and the adiabatic potential energy surfaces cross.

The seam of conical intersections and the point of the minimum energy conical intersection are shown in Figure 2 on a contour plot of the  $U_{22}$  diabatic potential energy surface in the  $\chi = 90^\circ$  coordinate plane. The point of minimum-energy conical intersection lies on the reactant side of the potential minimum, which is also located at  $\chi = 90^\circ$  and is marked by a cross in Figure 2. The minimum-energy conical intersection and the  $U_{22}$  minimum are located 0.372 and 0.360 eV above the  $M(ns) + H_2$  classical asymptote, respectively, and their geometries are listed in Table 1. The minimum-energy conical intersection coincides with the minimum-energy configuration on the excited-state adiabatic potential energy surface. At both the minimum-energy conical intersection and the minimum-energy point on  $U_{22}$ , the H–H bond is only slightly stretched from its equilibrium length in our model  $H_2$  diatomic molecule (by 0.004 and 0.002 Å, respectively) while the M–H bond is stretched significantly from its equilibrium value in the MH product (by 0.42 and 0.25 Å, respectively). Thus the minimum  $U_{22}$  structure shown in Figure 1 lies almost but not quite on the reaction path used for that figure.

At  $C_{2v}$  geometries derivatives of potential energy surfaces with respect to the  $\chi$  angle are equal zero by symmetry, and the gradient vector lies in the  $(R, r)$  coordinate plane. The gradients of the diabatic potential energy surfaces,  $\nabla U_{11}$  and  $\nabla U_{22}$ , calculated at the point of minimum-energy conical intersection are shown in Figure 2 by dashed and solid arrows, respectively. These vectors have opposite directions, and  $\nabla U_{11}$  is 5.5 times larger in the absolute magnitude than  $\nabla U_{22}$  since  $U_{11}$  changes much faster in this region (cf. Figure 1).

As mentioned above, the crossing seam is located on the reactant ( $M + H_2$ ) side of the  $U_{22}$  exciplex minimum. Because of that the ground-state adiabatic potential energy surface has an intermediate minimum separated from reactants by a small

**TABLE 1: Geometries, Energies, Vibrational Frequencies, and Vibrational Periods at Potential Minima**

surface	$R_{\text{MH}}$ (Å)	$R_{\text{MH}'}$ (Å)	$R_{\text{HH}}$ (Å)	$E$ (eV) <sup>a</sup>	$\omega_1$ (eV) (H–H)	$\omega_2$ (eV) (bend)	$\omega_3$ (eV) (M–H <sub>2</sub> )	$\tau_1$ (fs) (H–H)	$\tau_2$ (fs) (bend)	$\tau_3$ (fs) (M–H <sub>2</sub> )
$U_{22}$	1.59	1.59	0.749	0.360	0.3324	0.0689	0.0554	12.4	60.1	74.6
$V_1$	1.35	2.18	0.824	0.345	0.3469	0.0425 <sup>b</sup>	0.1363	11.9	97.5	30.3
$V_2$	1.72	1.72	0.751	0.372						

<sup>a</sup> Relative to the M(ns) + H<sub>2</sub> asymptote. <sup>b</sup> Doubly degenerate.

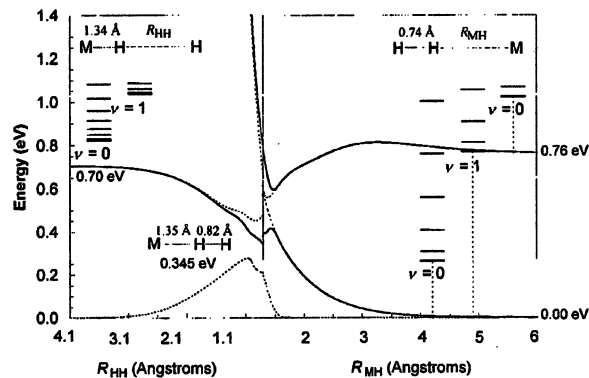


**Figure 3.** Diabatic (dashed lines) and adiabatic (solid lines) potential energy curves along an approximate reaction path confined to collinear ( $\chi = 0^\circ$ ) geometries (see text). Geometries and several lowest vibrational energy levels of the ground-state (M(ns) + H<sub>2</sub>) and the excited-state (M(ns) + H<sub>2</sub>) reactants, and of the products (MH + H) are also shown, as well as the geometry and classical energy of the minimum on the ground-state adiabatic potential energy surface.

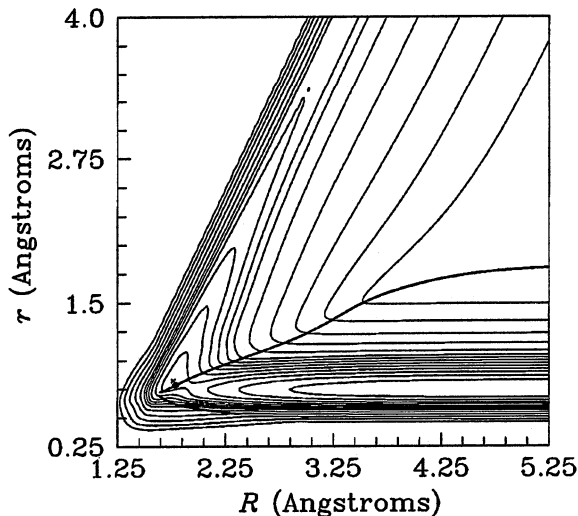


**Figure 4.** Contour plot of the excited-state adiabatic potential energy surface at collinear geometries. The seam of avoided crossings is shown by a thick solid line, the lowest-energy avoided crossing is shown by a solid dot, and the minimum is shown by a cross. The contour lines are 0.6, 0.7, 0.8, 0.9, 1.1, 1.4, 1.8, 2.3, and 2.9 eV.

barrier. This minimum is located at collinear,  $\chi = 0^\circ$ , geometry and its energy is equal to 0.345 eV relative to the ground-state M(ns) + H<sub>2</sub> classical asymptote. Diabatic and adiabatic potential energy curves along a reaction path similar to that of Figure 1 but confined to the  $\chi = 0^\circ$  coordinate plane are plotted in Figure 3, and Figure 4 contains a contour plot of the ground-state adiabatic potential energy surface for  $\chi = 0^\circ$ . On this figure we also marked the intermediate potential minimum discussed above, the seam of avoided crossing (defined for this plot as the curve along which  $U_{11} = U_{22}$ ), and the minimum-

energy point on this seam which is located at 0.362 eV. The energy gap between the adiabatic potential energy surfaces at the latter point is equal to 0.31 eV.

Contour plots of both diabatic and adiabatic potential energy surfaces in the ( $R_{\text{MH}}, R_{\text{HH}'}$ ) coordinate plane for M–H–H' bond angle fixed at 90° are shown in the supporting information for this paper.

Vibrational frequencies  $\omega_i$  (in energy units, i.e., multiplied by  $\hbar$ ) and the corresponding vibrational periods  $\tau_i$  at the minimum energy configuration on  $U_{22}$  and at the intermediate minimum on the ground-state potential energy surface are listed in Table 1. The vibrational periods are defined by

$$\tau_i = 2\pi/\omega_i \quad (4)$$

From this table we can see that the H–H vibrational mode in the exciplex is much faster than the M–H<sub>2</sub> Jacobi stretch and the bending modes which have vibrational frequencies 3–10 times smaller than the H–H vibrational frequency. Since the minimum on the upper adiabatic potential surface is located on the seam of conical intersection, vibrational frequencies are undefined at this minimum.

### 3. Accurate Quantum Dynamics

The quantum mechanical calculations were carried out by time-dependent scattering theory using the outgoing wave variational principle.<sup>9</sup> The problem was formulated in the diabatic electronic representation<sup>8,10</sup> as explained in detail elsewhere.<sup>11,12</sup> In this representation geometric phase effects<sup>13</sup> are included implicitly. The scattering wave function is a sum of a regular solution for a nonreactive rotationally coupled distortion potential<sup>14,15</sup> and an outgoing wave determined by the full potential. The complex outgoing wave is expanded in a multiarrangement basis set of total angular momentum eigenfunctions, symmetry adapted to take advantage of parity and A + B<sub>2</sub> homonuclear symmetry.<sup>16</sup>

The basis set consists of basis functions associated with asymptotic channels. In some convergence checks these were augmented by a set of basis functions associated with a two-dimensional grid in  $r, R$  space; each of these is a product of a two-dimensional gaussian in  $r, R$  times a rotational-orbital function in arrangement 1. However, the two-dimensional grid was not used for the final runs. Unlike the NaH<sub>2</sub> problem studied earlier, for the present problem faster convergence was achieved with only channel basis functions than with a combination of channel basis functions and basis functions defined on a two-dimensional grid. Each channel basis function consists of a linear combination of products of a channel internal function times a relative translational radial basis function. Each channel internal function is a product of an electronic ket,<sup>7,11,12</sup> a diatomic vibrational–rotational function, a spherical harmonic for atom–diatom orbital motions.<sup>12</sup> The relative translational radial basis functions are taken as channel components of rotationally coupled half-integrated Green's functions<sup>17,18</sup> or distributed gaussians<sup>19</sup> in open channels and as distributed gaussians in closed channels.

The regular functions and half-integrated Green's functions are determined by the finite difference boundary value method with high-order (11-point) finite difference operators.<sup>15</sup> Matrix elements over the basis functions are determined by a combination of angular momentum algebra and multidimensional numerical integration involving products of repeated Gauss-Legendre quadratures.<sup>11</sup> The coupled equations for the coefficients of the basis functions and scattering matrix elements are reduced<sup>11,20</sup> to a large real set of equations solved by the  $UDU^T$  algorithm<sup>21</sup> and a smaller complex set of equations solved by our complex implementation of the standard<sup>22</sup> LU decomposition algorithm.

#### 4. TSH Methods

The two basic variants of TSH that we studied are Tully's fewest switches<sup>3</sup> (TFS) algorithm and the Blais-Truhlar<sup>4</sup> (BT) algorithm. Full details of both methods are presented elsewhere.<sup>3-5,23</sup> The coupled equations for coordinates, momenta, electronic state coefficients, and phases were integrated by the Bulirsch-Stoer method<sup>2,24</sup> with polynomial extrapolation. The equations for the electronic state coefficients and phases involve the momentum coupling matrix elements in the adiabatic representation and these were obtained from the derivatives of the diabatic Hamiltonian matrix elements by the method of Preston and Tully,<sup>25</sup> which is exact for our model. Final-state analysis was based on the histogram method as discussed elsewhere.<sup>23</sup>

The original TSH method,<sup>26</sup> due to Tully and Preston, involved predefined crossing seams where the hopping probability was calculated by the Landau-Zener expression with parameters fit to numerical solutions of the coupled equations for the complex adiabatic state coefficients. Hopping was only allowed at the preidentified seams, and the momentum was adjusted in the component normal to the seam.

The two methods<sup>4,5</sup> examined here both allow for hops at any position in space, and they are based on integrating the coupled equations for the complex adiabatic state coefficients along with the trajectories. No fitting is required, and no particular topography of the surfaces is assumed. Thus the methods are not even restricted to localized seams. At any given point in space and time, the probability of being on surface  $i$  is given by

$$P_i(t) = |a_i(t)|^2 \quad (5)$$

where  $t$  is the time.

The BT method always integrates the classical equations on a surface  $i$  with  $P_i(t) > 0.5$ . When this probability falls to 0.5, a surface hop decision is made on the basis of random number, and the complex state coefficient for the new surface (which may be the same as the old surface) is reinitialized to unity. Tully's fewest-switches method allows hops for any value of  $P_i(t)$ , and the hopping probability is determined by the requirement that one makes the fewest "switches" (i.e., hops) consistent with an algorithm in which the ensemble average of fractional state populations converges to the set of  $P_i(t)$ . The state coefficients are not reinitialized after hops. As a result, a trajectory may propagate for long periods of time on a surface for which  $P_i(t) \ll 0.5$ .

The TSH algorithms require specifying a direction  $\vec{N}$  such that, when a hop occurs, the momentum required to be added or withdrawn from nuclear motion to conserve total energy is added or subtracted in the component parallel to  $\vec{N}$ .<sup>23,27</sup> The direction  $\vec{N}$  may be considered to represent a normal to a step

TABLE 2: Reaction and Quenching Probabilities for Collisions of M(np) with H<sub>2</sub>(v = 0, j = 0 or 2)<sup>a</sup>

$j$	method	reaction probability	nonreactive quenching probability	sum <sup>b</sup>
0	quantum	0.80	0.07	0.87
	BT-g	0.47	0.29	0.76
	TFS-g	0.68	0.22	0.90
	BT-d	0.46	0.29	0.76
	TFS-d	0.68	0.20	0.88
2	quantum	0.72	0.19	0.91
	BT-g	0.46	0.39	0.85
	TFS-g	0.64	0.30	0.94
	BT-d	0.45	0.40	0.85
	TFS-d	0.66	0.27	0.94

<sup>a</sup> For trajectory surface hopping results the standard deviations are less than 0.01 in all cases. <sup>b</sup> Summed before rounding.

in the potential energy surface corresponding to the hop. In our previous paper,<sup>3</sup> following ref 4, we set  $N$  equal to  $\vec{g}/|\vec{g}|$  where

$$\vec{g} \equiv \vec{\nabla}(V_2 - V_1) \quad (6)$$

Thus  $\vec{g}$  is the gradient of the gap. An alternative choice that has been proposed<sup>5,28</sup> for the direction  $N$  is the nonadiabatic coupling direction  $\vec{d}/|\vec{d}|$ , where

$$\vec{d} = \langle 1 | \vec{\nabla} | 2 \rangle \quad (7)$$

and where  $|1\rangle$  and  $|2\rangle$  denote the adiabatic electronic wave functions. In the present work we study both TSH algorithms with both choices of  $N$ . This yields four variants labeled TFS-g, TFS-d, BT-g, and BT-d.

#### 5. Calculations

We consider  $v = 0$  and  $j = 0$  and 2 in eq 1, total energy  $E = 1.10$  eV [where  $E$  is measured with respect to M(ns) infinitely far from H<sub>2</sub> without zero-point energy and at its classical equilibrium separation], and total angular momentum  $J = 0$ . For the  $j = 0$  initial state, the initial relative translational energy  $E_{int}$  is 0.076 eV, and the initial relative translational orbital angular momentum  $l$  is 0. For the  $j = 2$  initial state,  $E_{int}$  is 0.032 eV and  $l$  is 2.

The quantum mechanical state-to-state transition probabilities were converged to 1% or better with respect to all basis set and numerical parameters. Our final results are based on a calculation with 34 open channels and 323 closed channels. The channel basis set used for the outgoing wave contains 30–31 coupled-channel half-integrated Green's functions in each open channel and 30–31 single-channel distributed Gaussians in each closed channel. Further details of the basis set and numerical parameters are given in the supporting information, along with the results of convergence checks.

For each of the four variants of TSH, and for each of the two initial states, we calculated 6000 trajectories with local absolute truncation error of  $10^{-12}$  and minimum step size  $10^{-4} a_0$ . Trajectories were started with the atom at least  $\rho = 13.2$  Å from the diatom and were propagated until the final atom-diatom distance exceeded  $\rho' = 13.2$  Å. The results are well-converged with respect to varying these parameters.

#### 6. Results and Discussion

Quantum mechanical transition probabilities, summed over final rotational states for a given initial state, process, and final vibrational quantum number, are presented in Table 2. The

**TABLE 3: Average Vibrational and Rotational Quantum Numbers and Transition Probabilities for Producing a Given Vibrational Level for Collisions of M(np) with H<sub>2</sub>(v = 0, j = 0 or 2)<sup>a</sup>**

j	product	method	probability of a given final vibrational state <sup>b</sup>			
			<v'> or <v''>"	<j'> or <j''>"	v' or v'' = 0	v' or v'' = 1
0	MH + H	quantum	0.35	4.5	0.52	0.28
		BT-g	0.34	5.8	0.31	0.16
		TFS-g	0.41	5.3	0.40	0.28
		BT-d	0.33	5.8	0.31	0.15
		TFS-d	0.40	5.4	0.41	0.27
0	M(ns) + H <sub>2</sub>	quantum	0.72	3.9	0.02	0.05
		BT-g	0.07	0.8	0.27	0.02
		TFS-g	0.07	1.1	0.21	0.01
		BT-d	0.07	1.1	0.28	0.02
		TFS-d	0.07	1.0	0.19	0.01
2	MH + H	quantum	0.34	5.1	0.47	0.24
		BT-g	0.37	5.4	0.29	0.17
		TFS-g	0.33	5.8	0.43	0.21
		BT-d	0.40	5.4	0.27	0.18
		TFS-d	0.33	5.6	0.44	0.22
2	M(ns) + H <sub>2</sub>	quantum	0.29	3.2	0.14	0.06
		BT-g	0.11	4.9	0.35	0.05
		TFS-g	0.15	5.2	0.25	0.05
		BT-d	0.13	4.6	0.35	0.05
		TFS-d	0.17	4.9	0.23	0.05

<sup>a</sup> For trajectory surface-hopping results: standard deviations are less than or equal to 1 in last digit quoted in all cases. <sup>b</sup> Summed over rotational states.

same transition probabilities obtained from TSH calculations are also shown in this table and can be compared to the quantum ones.

In the system studied here chemical reaction and quenching occur only in electronically nonadiabatic collisions. Table 2 shows that 87–91% of the collisions are electronically nonadiabatic, depending on the initial rotational state. The TFS algorithm yields 88–94% for this quantity, in excellent agreement with accurate quantum dynamics, while the BT algorithm yields only 76–85%, significantly worse. The branching of this flux into reactive and quenching probabilities provides a steeper test of the semiclassical theories. The accurate branching ratio is about 12 for  $j = 0$  and 4 for  $j = 2$ . The TFS algorithm yields about 3 and 2, respectively, while BT algorithm yields about 1.6 and 1.1, respectively. Although neither algorithm is quantitatively accurate the TFS algorithm is closer to accurate quantum dynamics. An analysis of the trajectories in the BT calculations showed that under the conditions studied here, less than 17% of the trajectories reflect without ever reaching a surface hop decision.

First moments of  $v''$  and  $j''$  for quenching collisions and of  $v'$  and  $j'$  for reactive collisions are given in Table 3. This table tests the ability of the semiclassical methods to predict final state distributions. The partitioning of flux into ground and excited vibrational states for reactive collisions is predicted quite well. In particular, the average values of the MH final vibrational quantum number for the accurate, TFS, and BT cases are, respectively, 0.35, 0.40, and 0.34 for  $j = 0$  and 0.34, 0.33, and 0.39 for  $j = 2$ . Agreement between average final vibrational quantum numbers is summarized in Table 4; it is much worse in the more quantum (due to the higher vibrational frequency and rotational constant of H<sub>2</sub> compared to MH) M + H<sub>2</sub> channel with an error equal to about 90% for  $j = 0$  and  $50 \pm 10\%$  for the  $j = 2$  initial state. The rotational partitioning is on average not well reproduced. For the  $j = 0$  initial state the average rotational quantum numbers obtained from trajectory calcula-

**TABLE 4: Average Deviations of First Moments of Product Vibrational Distributions from Accurate Quantum Ones<sup>a</sup>**

	j = 0	j = 2
reaction		
BT	3%	14%
TFS	16%	2%
nonreactive quenching		
BT	90%	58%
TFS	91%	46%

<sup>a</sup> Average of g and d prescriptions.

**TABLE 5: Total Quenching Probability from Statistical Calculation**

$\lambda_E$ (eV)	$\lambda_R$ (Å)	$R_c$ (Å)	$k_{\text{dis}}$ (ps <sup>-1</sup> )	$k_{\text{crit}}$ (ps <sup>-1</sup> )	$k_{\text{quench}}$ (ps <sup>-1</sup> )	quenching probability
0.005	0.0053	5.8	$1.16 \pm 0.06$	$29.1 \pm 0.3$	$25.2 \pm 0.3$	$0.96 \pm 0.02$
0.005	0.0053	7.5	$0.99 \pm 0.07$	$22.3 \pm 0.3$	$19.3 \pm 0.3$	$0.95 \pm 0.03$
0.005	0.0053	9.0	$0.76 \pm 0.06$	$18.6 \pm 0.3$	$16.1 \pm 0.3$	$0.95 \pm 0.04$
0.003	0.0053	5.8	$1.18 \pm 0.02$	$29.8 \pm 0.1$	$25.8 \pm 0.1$	$0.96 \pm 0.01$
0.003	0.0053	7.5	$0.94 \pm 0.02$	$23.1 \pm 0.2$	$20.0 \pm 0.2$	$0.96 \pm 0.02$
0.003	0.0053	9.0	$0.75 \pm 0.02$	$19.1 \pm 0.2$	$16.5 \pm 0.2$	$0.96 \pm 0.02$
0.003	0.0026	7.5	$0.93 \pm 0.02$	$23.1 \pm 0.2$	$20.0 \pm 0.2$	$0.96 \pm 0.02$

tions deviate from the corresponding quantum mechanical values by 16–28% for reactive collisions and by 72–79% for nonreactive quenching. The deviations are slightly smaller for the  $j = 2$  initial state: 4–12% and 41–62%, respectively.

The tables and figures show very little difference between the two criteria for adjusting the momentum, so in further discussion of the results we will usually consider the average of the g and d prescriptions.

In order to understand the probability of nonadiabatic events better we carried out a statistical calculation, using the new statistical method we have recently presented<sup>29</sup> for strongly coupled diabatic surfaces (weakly coupled adiabatic surfaces). In this method the quenching probability is equal to the ratio of the quenching rate constant,  $k_{\text{quench}}(E, J)$ , to the total rate constant for the decay of the exciplex that is equal to the sum of the quenching rate constant and rate constant for the dissociation of the exciplex back to the reactants without deexcitation,  $k_{\text{dis}}(E, J)$ ,

$$P_Q(E, J) = \frac{k_{\text{quench}}(E, J)}{k_{\text{quench}}(E, J) + k_{\text{dis}}(E, J)} \quad (8)$$

The quenching and dissociation rate coefficients were obtained by performing numerically the microcanonical phase-space averaging of the corresponding fluxes.<sup>29</sup> For  $j = 0$  or 2, there is essentially no barrier in the entrance channel, and therefore, the quenching probability depends slightly on the position  $R_c$  of the dividing surface separating exciplex from the electronically excited reactants M(np) + H<sub>2</sub>. Table 5 contains the results for several different values of  $R_c$ . Parameters  $\lambda_E$  and  $\lambda_R$  in Table 5 are numerical parameters which should be sufficiently small for the calculation to converge. Table 5 demonstrates that our results are converged with respect to these parameters.

The statistical calculation predicts 96% nonadiabatic processes. It is not clear how to divide this between reactive and quenching probabilities, but statistically half the quenching would have negative M-to-H<sub>2</sub> momentum and half would have positive M-to-H<sub>2</sub> momentum. One would expect all the former ones and some nonzero fraction of the latter to lead to M(ns) + H<sub>2</sub>. Thus the statistical reaction-to-quenching ratio would be  $\leq 1$ . Thus the statistical model cannot explain the observed branching ratios.

Further insight into the statisticality of the collisions, or lack thereof, can be obtained from the lifetime distributions of

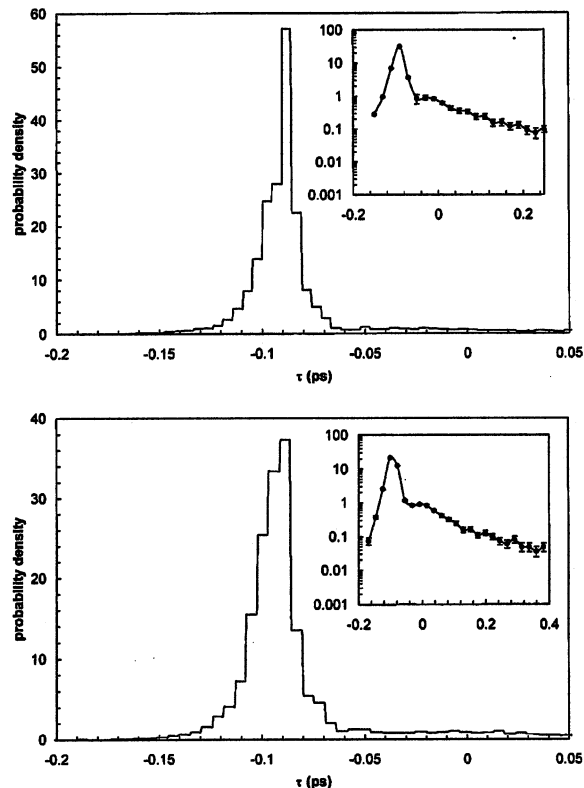


**Figure 5.** Distribution (histogram) of collision lifetimes for the  $\nu = 0, j = 0$  initial state. Part a, BT method; part b, TFS method. Inserts show the same distribution on logarithmic scale.

quenched trajectories (i.e., trajectories that end on the ground electronic state) in Figure 5. Distributions calculated for the  $j = 0$  initial state with the BT and TFS methods are presented in Figures 5a,b, respectively. The plots for  $j = 2$  are similar to those for  $j = 0$  and so are not shown. The collision lifetime of a trajectory is defined as<sup>30</sup>

$$\begin{aligned} \tau(\rho, \rho', E, J, \dots) &\equiv \lim_{\rho \rightarrow \infty} [T(\rho, \rho', E, J, \dots) - T_0(\rho, \rho', E, J, \dots)] \\ &= \lim_{\rho' \rightarrow \infty} [T(\rho, \rho', E, J, \dots) - \rho/\nu_{\text{rel}} - \rho'/\nu'_{\text{rel}}], \quad (9) \end{aligned}$$

where  $\rho$  is the initial separation between M(np) and H<sub>2</sub>,  $\rho'$  is the final separation between M(ns) and H<sub>2</sub> or MH and H',  $\nu_{\text{rel}}$  and  $\nu'_{\text{rel}}$  are initial and final relative velocities,  $T$  is the time of the collision, and  $T_0$  is the time that the particles would have spent between the initial and final points of the trajectory in the absence of interaction potential. Due to the repulsive part of the potential at short internuclear distances, most of the trajectories have negative collision lifetimes. As discussed in section 2 the seam of conical intersection and the hyperplane of avoided crossings are located on the reactant side of the exciplex minimum on the  $U_{22}$  diabatic potential energy surface (see Figures 1–4). This can be compared to the NaH<sub>2</sub> system studied earlier<sup>3</sup> where the minimum-energy conical intersection almost coincided with the  $U_{22}$  minimum. Because the  $U_{12}$  function dies off rapidly as we move from the interaction region to the reactant asymptote, the diabatic coupling is relatively weak at the seam of crossing between  $U_{11}$  and  $U_{22}$  surfaces even for

**TABLE 6: Quenching Rates from Collision Lifetime Distributions of Quenching Trajectories**

initial state	method	$k(E, J)$ (ps <sup>-1</sup> )	number of statistical trajectories (%)
$\nu = 0, j = 0$	BT	$9.9 \pm 0.6$	$7.8 \pm 0.3$
	TFS	$11.3 \pm 0.7$	$9.5 \pm 0.3$
$\nu = 0, j = 2$	BT	$10.3 \pm 0.3$	$15.3 \pm 0.4$
	TFS	$12.9 \pm 0.5$	$13.5 \pm 0.3$

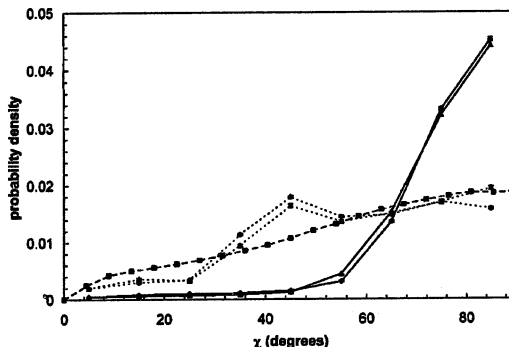


**Figure 6.** Distribution (histogram) of the angle  $\chi$  at the moment of hopping. Triangles, BT method; diamonds, TFS method. Filled markers connected by solid line correspond to the  $\nu = 0, j = 0$  initial state, hollow markers connected by short-dashed lines correspond to the  $\nu = 0, j = 2$  initial state. Results of the statistical model are shown by the squares connected by long-dashed lines.

$\chi < 90^\circ$  as compared to the NaH<sub>2</sub> system.<sup>3</sup> A typical trajectory from the left part of the lifetime distribution changes electronic surfaces at its first crossing of the seam region, and then directly proceeds toward the MH + H' asymptote. Obviously, such trajectories are poorly described by a statistical model which assumes that the system is trapped for a long time in the exciplex well and gets completely randomized. Trajectories from the long-lifetime tail of the distribution spend more time in the exciplex well, and the statistical model might be applicable to this part of the distribution. For unimolecular statistical decay of a complex<sup>31,32</sup> the lifetime distribution is exponential

$$P(E, J, \tau) = k(E, J) \exp[-k(E, J)\tau] \quad (10)$$

and can be used to extract the unimolecular rate constant,  $k(E, J)$ .<sup>29</sup> Indeed, within the numerical error bars of our calculation, the large- $\tau$  part of the lifetime distributions in Figure 5 can be fit to the exponential function of eq 10. Table 6 lists the fraction of trajectories belonging to the exponential part of the lifetime distribution and the resulting exponents,  $k(E, J)$ , which in this case give the quenching rates,  $k_{\text{quench}}(E, J)$ . On average the quenching rates are equal to about 11 ps<sup>-1</sup>, and only about 10% of trajectories lie in the region of the lifetime distribution that is linear on the logarithmic plots of probability density vs.  $\tau$  shown as inserts in Figure 5. By comparing Tables 5 and 6 we can see that our statistical model overestimates the rate of quenching by at least a factor of 2. This is similar to the results for the Na(3p) + H<sub>2</sub> nonreactive collisions<sup>29</sup> where the statistical model also predicted quenching rates 2–3 times larger than those extracted from trajectory lifetime distributions. The discrepancy can be explained by the neglect of multiple electronic transitions in the statistical calculation, although the above analysis of the lifetime distributions indicates that statistical approximation itself is completely inadequate for the present system.

Figure 6 shows the distribution of hops as a function of scattering angle as obtained from trajectory calculations and from the statistical model. Figure 7 is similar to Figure 6 but

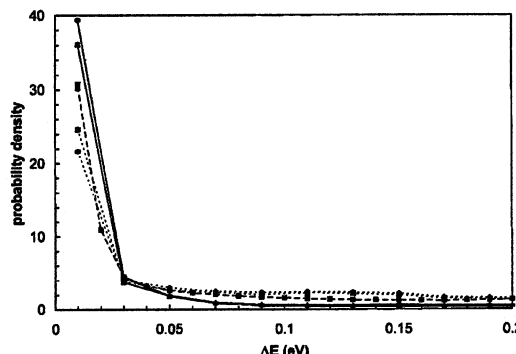


**Figure 7.** Distribution (histogram) of the energy gap ( $\Delta E$ ) between the adiabatic potential energy surfaces at the moment of hopping. Triangles, BT method; diamonds, TFS method. Filled markers connected by solid line correspond to the  $v = 0, j = 0$  initial state, hollow markers connected by short-dashed lines correspond to the  $v = 0, j = 2$  initial state. Results of the statistical model are shown by the squares connected by long-dashed lines.

for the hopping distribution as a function of the adiabatic energy gap at the hop location. The hopping distributions obtained with two TSH methods agree with each other very well. However, there is a large difference, especially for angular distributions, between the  $j = 0$  and the  $j = 2$  results. For  $j = 0$  the probability of electronic transitions increases monotonically with  $\chi$ , and the distributions look very similar to the ones obtained earlier for  $\text{Na}(3p) + \text{H}_2$  nonreactive collisions.<sup>29</sup> For  $j = 2$  the angular distributions have higher probability at small values of  $\chi$  compared to the  $j = 0$  case, and they actually have a maximum at  $\chi \approx 45^\circ$ . The difference between the  $j = 0$  and the  $j = 2$  cases is not caused by the difference in the translational energy because an additional  $j = 2$  calculation with the same relative translational energy as for the  $j = 0$  case (0.076 eV translational energy and 1.143 eV total energy) produced distributions similar to those from the original  $j = 2$  calculation (with translational energy of 0.032 eV). As discussed above, most trajectories in this system are nonstatistical (i.e., they hop to the ground electronic surface and leave the interaction region right after they reach the crossing seam for the first time during their initial approach from the reactant asymptote). Therefore, the angular hopping distributions are probably strongly influenced by the angular distributions of trajectories in the reactant channel. This explains larger differences between the trajectory results and the predictions of the statistical model than those observed for the  $\text{Na}(3p) + \text{H}_2$  nonreactive collisions<sup>29</sup> where about half of all trajectories were “statistical” (as opposed to about 10% for the present system). We note that initial distributions of reactants with respect to the angle  $\chi$  are quite different for the  $j = 0$  and the  $j = 2$  initial state because of the difference in the distribution of the impact parameter corresponding to the  $l = 0$  and the  $l = 2$  cases ( $l = j$  for  $J = 0$ , where  $l$  is the orbital angular momentum quantum number).<sup>33</sup> This difference in initial  $\chi$ -distributions might also be the cause of the difference between angular hopping distributions for the two initial rotational states.

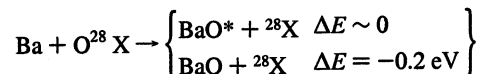
## 7. Concluding Remarks

For single-surface (electronically adiabatic) reaction dynamics quasiclassical trajectory methods have been extensively tested vs quantum mechanical results (for some of the most recent work see, e.g., refs 34–46). In general, agreement between quantum mechanical and quasiclassical trajectories is quite good,

although such problems as the inability of trajectory calculations to account for tunneling effects and zero-point energy restrictions can lead to large errors for some systems. On average the errors are smaller for heavier particles, for more averaged quantities, and further from energetic thresholds and quantum resonances.<sup>23</sup>

Here and in our previous paper<sup>3</sup> on nonreactive quenching collisions of  $\text{Na}(3p)$  and  $\text{H}_2$  we extend the comparison of quantum mechanical and trajectory methods to the case of electronically nonadiabatic reactions. For both nonadiabatic systems that we have studied (the present one and the  $\text{Na}(3p) + \text{H}_2$  quenching collisions<sup>3</sup>) trajectory surface hopping methods seem to be able to predict average quenching probabilities at least qualitatively correctly (although, unsurprisingly, oscillations of quantum mechanical probabilities as functions of energy could not be reproduced<sup>3</sup>). However, unlike the nonreactive collisions of ref 3, the reactive system studied here presents an opportunity to test the ability of TSH methods to predict more detailed information such as the branching ratios between the two different product channels.

Although there are no previous tests of the TSH method for reactive collisions in 3-D, there is a relevant previous test for a collinear system. In particular Bowman et al. studied<sup>47</sup> the system



where  ${}^{28}\text{X}$  is pseudoatom of mass 28 and \* denotes electronic excitation. For a relative translational energy  $E_{\text{rel}}$  in the range of 0.1 eV, the probability of producing  $\text{BaO}^*$  was (on average) 0.3 quantum mechanically but only 0.1 when calculated by the original Tully-Preston TSH method. The authors concluded that the TSH model was inadequate, despite the large masses of all nuclei.

One expects that semiclassical methods will often improve in larger numbers of dimensions because of increased averaging, and in the present case we find errors in the electronically nonadiabatic reaction probabilities of only 9–15% for the TFS algorithm and ~40% for the BT algorithm, as compared to 67% for the collinear example. However, our nonreactive quenching probabilities have more than 200% errors for  $j = 0$  and 40–100% errors for  $j = 2$ , and the branching ratios are off by a factor of 3.5–7.7 for  $j = 0$  and factors of 1.5–3.3 for  $j = 2$ . The reaction probabilities have smaller relative errors in our case than in ref 47 because these probabilities are closer to 1. But the absolute errors in the reaction probabilities are comparable (0.12–0.34 for  $j = 0$  and 0.06–0.27 for  $j = 2$ ). Thus, despite the “good” agreement with accurate quantum dynamics for the total nonadiabatic reaction probability, many of the state-selected results are not well reproduced by TSH, although errors are smaller for the  $j = 2$  state than for the highly quantum  $j = 0$  one. Especially for  $j = 0$ , the present results are no better than those of ref 47. In general for the present reactive system, the overall agreement between the results of trajectory surface hopping and accurate quantum mechanical calculations seems to be worse than for the nonreactive quenching collisions studied in ref 3. Further testing on a variety of systems will be required to assess the generality of the qualitative trends.

We have also used a previously developed statistical model to calculate the rate constants for the unimolecular decay of the exciplex and the overall quenching probabilities. The statistical quenching rates constants differ from those obtained from TSH calculations by at least a factor of 2, which is not surprising since our analysis of the collision time distributions of the trajectories showed that about 90% of them hop to the

ground electronic state at their first passage of the crossing seam and proceed directly to products without getting trapped in the exciplex well.

**8. Acknowledgments** This work was supported in part by the National Science Foundation under Grant no. CHE94-23927.

**Supporting Information Available:** Functional forms and parameters of potential energy surfaces, additional contour plots, parameters and convergence tests for accurate quantum scattering calculations, and converged values of the state-to-state cross sections (23 pages). Ordering information is given on any current masthead page.

## References and Notes

- (1) For reviews, see: (a) Tully, J. C. In *Dynamics of the Molecular Collisions, Part B*; Miller, W. H., Ed.; Plenum: New York, 1976; p 217. (b) Tully, J. C. *ACS Symp. Ser.* **1977**, *56*, 206. (c) Chapman, S. *Adv. Chem. Phys.* **1992**, *82*, 423.
- (2) Parlant, G.; Alexander, M. H. *J. Chem. Phys.* **1989**, *91*, 4416; **1990**, *92*, 2287.
- (3) Topaler, M. S.; Hack, M.-D.; Allison, T. C.; Liu, Y.-P.; Mielke, S. L.; Schwenke, D. W.; Truhlar, D. G. *J. Chem. Phys.* **1997**, *106*, 8699.
- (4) (a) Blais, N. C.; Truhlar, D. G. *J. Chem. Phys.* **1983**, *79*, 1334. (b) Blais, N. C.; Truhlar, D. G.; Mead, C. A. *J. Chem. Phys.* **1988**, *89*, 6204.
- (5) Tully, J. C. *J. Chem. Phys.* **1990**, *93*, 1061.
- (6) Halvick, P.; Truhlar, D. G. *J. Chem. Phys.* **1992**, *96*, 2895.
- (7) Schwenke, D. W.; Mielke, S. L.; Tawa, G. J.; Friedman, R. S.; Halvick, P.; Truhlar, D. G. *Chem. Phys. Lett.* **1993**, *203*, 565.
- (8) Mead, C. A.; Truhlar, D. G. *J. Chem. Phys.* **1982**, *77*, 6090.
- (9) Sun, Y.; Kouri, D. J.; Truhlar, D. G.; Schwenke, D. W. *Phys. Rev. A* **1990**, *41*, 4857.
- (10) (a) Garrett, B. C.; Truhlar, D. G. *Theor. Chem. Adv. Perspect.* **1981**, *6A*, 1. (b) Baer, M. In *Theory of Chemical Reaction Dynamics*; Baer, M., Ed.; CRC Press: Boca Raton, 1985; Vol. 2, pp 219–280.
- (11) Tawa, G. J.; Mielke, S. L.; Truhlar, D. G.; Schwenke, D. W. In *Advances in Molecular Vibrations and Collision Dynamics*; Bowman, J. M., Ed.; JAI Press: Greenwich, CT, 1994; Vol. 2B, pp 45–116.
- (12) Tawa, G. J.; Mielke, S. L.; Truhlar, D. G.; Schwenke, D. W. *J. Chem. Phys.* **1994**, *100*, 5751.
- (13) Mead, C. A.; Truhlar, D. G. *J. Chem. Phys.* **1979**, *70*, 2284.
- (14) Schwenke, D. W.; Haug, K.; Zhao, M.; Truhlar, D. G.; Sun, Y.; Zhang, J. Z. H.; Kouri, D. J. *J. Phys. Chem.* **1988**, *92*, 3202.
- (15) Mielke, S. L.; Truhlar, D. G.; Schwenke, D. W. *J. Chem. Phys.* **1991**, *95*, 5930.
- (16) Schwenke, D. W.; Mladenovic, M.; Zhao, M.; Truhlar, D. G.; Sun, Y.; Kouri, D. J. In *Supercomputer Algorithms for Reactivity, Dynamics, and Kinetics of Small Molecules*; Lagana, A., Ed.; Kluwer: Dordrecht, 1989; pp 131–168.
- (17) Zhang, J. Z. H.; Kouri, D. J.; Haug, K.; Schwenke, D. W.; Shima, Y.; Truhlar, D. G. *J. Chem. Phys.* **1988**, *88*, 2492.
- (18) Sun, Y.; Kouri, D. J.; Truhlar, D. G. *Nucl. Phys.* **1990**, *A508*, 41c.
- (19) Hamilton, I. P.; Light, J. C. *J. Chem. Phys.* **1986**, *84*, 306.
- (20) Schwenke, D. W.; Truhlar, D. G. In *Computing Methods in Applied Sciences and Engineering*; Glowinski, R., Lichnewsky, A., Eds.; SIAM: Philadelphia, 1990; pp 291–310.
- (21) Anderson, E.; Bai, Z.; Bischof, C.; Demmel, J.; Dongarra, J. J.; Du Croz, J.; Greenbaum, A.; Hammarling, S.; McKenney, A.; Ostrouchov, S.; Sorenson, D. *LAPACK Users' Guide*; SIAM: Philadelphia, 1992; pp 203–205.
- (22) Dongarra, J. J.; Bunch, J. R.; Moler, C. B.; Stewart, G. W. *LINPACK Users' Guide*; SIAM: Philadelphia, 1973; pp C.75–C.82.
- (23) Truhlar, D. G.; Muckerman, J.-T. In *Atom-Molecule Collision Theory*; Bernstein, R. B., Ed.; Plenum: New York, 1979; pp 505–566.
- (24) Stoer, J.; Bulirsch, R. *Introduction to Numerical Analysis*; Springer Verlag: New York, 1980.
- (25) Preston, R. K.; Tully, J. C. *J. Chem. Phys.* **1971**, *54*, 4297.
- (26) Tully, J. C.; Preston, R. K. *J. Chem. Phys.* **1971**, *55*, 562.
- (27) Miller, W. H.; George, T. F. *J. Chem. Phys.* **1972**, *56*, 5637.
- (28) Herman, M. F. *J. Chem. Phys.* **1984**, *81*, 754.
- (29) Topaler, M. S.; Truhlar, D. G. *J. Chem. Phys.* **1997**, *107*, 392.
- (30) Smith, F. T. *Phys. Rev.* **1960**, *118*, 349.
- (31) Bunker, D. L. *Theory of Elementary Gas Reaction Rates*; Pergamon: New York, 1966.
- (32) Hase, W. H. In *Potential Energy Surfaces and Dynamics Calculations*; Truhlar, D. G., Ed.; Plenum: New York, 1981; pp 1–35.
- (33) See ref 23 for a detailed description of how initial conditions were sampled in our TSH calculations.
- (34) Blais, N. C.; Zhao, M.; Mladenovic, M.; Truhlar, D. G.; Schwenke, D. W.; Sun, Y.; Kouri, D. J. *J. Chem. Phys.* **1989**, *107*, 392.
- (35) Blais, N. C.; Zhao, M.; Truhlar, D. G.; Schwenke, D. W.; Kouri, D. J. *Chem. Phys. Lett.* **1990**, *166*, 11.
- (36) Zhao, M.; Truhlar, D. G.; Blais, N. C.; Schwenke, D. W.; Kouri, D. J. *Phys. Chem.* **1990**, *94*, 6696.
- (37) Neuhauser, D.; Judson, R. S.; Jaffe, R. L.; Baer, M.; Kouri, D. J. *Chem. Phys. Lett.* **1991**, *176*, 546.
- (38) Rosenman, E.; Hochman-Kowal, S.; Persky, A.; Baer, M. *J. Phys. Chem.* **1995**, *99*, 16523.
- (39) Gilibert, M.; Blasco, R. M.; Gonzalez, M.; Gimenez, X.; Aguilar, A.; Last, I.; Baer, M. *J. Phys. Chem.* **1997**, *101*, 6821.
- (40) Aoiz, F. J.; Bafaires, L.; D'Mello, M. J.; Sáez Rábano, V.; Schneider, L.; Wyatt, R. E. *J. Chem. Phys.* **1994**, *101*, 5781.
- (41) Aoiz, F. J.; Bafaires, L.; Martínez-Haya, B.; Castillo, J. F.; Manolopoulos, D. E.; Stark, K.; Werner, H.-J. *J. Phys. Chem. A* **1997**, *101*, 6403.
- (42) Jakubetz, W.; Sokolovski, D.; Connor, J. N. L.; Schatz, G. C. *J. Chem. Phys.* **1992**, *97*, 6451.
- (43) Goldfield, E. M.; Gray, S. K.; Schatz, G. C. *J. Chem. Phys.* **1995**, *102*, 8807.
- (44) Schatz, G. C.; Lendvay, G. *J. Chem. Phys.* **1997**, *106*, 3548.
- (45) Clary, D. C.; Schatz, G. C. *J. Chem. Phys.* **1993**, *99*, 4578.
- (46) Palma, J.; Echave, J.; Clary, D. C. *C. R. Acad. Sci. Paris, Ser. II, Phys. Chim. Biophys.* **1997**, *322*, 841.
- (47) Bowman, J. M.; Leisure, S. C.; Kuppermann, A. *Chem. Phys. Lett.* **1976**, *43*, 374.

September 29, 1997

Supporting Information for

**Test of Trajectory Surface Hopping Against Accurate Quantum Dynamics for Electronically Nonadiabatic Chemical Reactions**

Maria S. Topaler,<sup>a</sup> Thomas C. Allison,<sup>a</sup> David W. Schwenke,<sup>b</sup> and Donald G. Truhlar<sup>a</sup>

<sup>a</sup>*Department of Chemistry and Supercomputer Institute, University of Minnesota, Minneapolis, MN 55455-0431*

<sup>b</sup>*NASA Ames Research Center, Mail Stop 230-3, Moffett Field, CA 94035-1000*

**S.1. Functional form of potential energy surfaces**

The two diabatic surfaces,  $U_{11}$  and  $U_{22}$ , are given by the following functional forms

$$U_{11} = Q_{\text{HH},1} + Q_{\text{MH},1} + Q_{\text{MH}',1} - \frac{1}{\sqrt{2}} \sqrt{W_1 + c_1^2} + D_e(\text{H}_2), \quad (\text{S1})$$

$$\begin{aligned} U_{22} = & (Q_{\text{HH},2} + Q_{\text{MH},2} + Q_{\text{MH}',2} - \frac{1}{\sqrt{2}} \sqrt{W_2 + c_2^2} + D_e(\text{H}_2) - \Delta E_1) \\ & / \left( 1 + \Delta E_2 \{1 - \Theta[d(R_{\text{NaH}} - \Delta R_{\text{NaH}})]\Theta[d(R_{\text{NaH}'} - \Delta R_{\text{NaH}}')] \} \right). \end{aligned} \quad (\text{S2})$$

The functions in Eqs. (S1) and (S2) are defined as follows:

$$W_i = (J_{\text{HH},i} - J_{\text{MH},i})^2 + (J_{\text{MH},i} - J_{\text{MH}',i})^2 + (J_{\text{HH},i} - J_{\text{MH}',i})^2, \quad (\text{S3})$$

$$Q_{\text{AB},i} = \frac{1}{2}(S_{\text{AB},i} + T_{\text{AB},i}), \quad (\text{S4})$$

$$J_{\text{AB},i} = \frac{1}{2}(S_{\text{AB},i} - T_{\text{AB},i}), \quad (\text{S5})$$

where A, B = M, H, or H' (A ≠ B),

$$c_i = c_{ia} \exp[-c_{ib} W_i - c_{ic} (2/3 R_{\text{HH}'} + R_{\text{MH}} + R_{\text{MH}'})], \quad (\text{S6})$$

$$d_{\text{NaH}} = d_{\text{NaH}}^{as} + (d_{\text{NaH}}^{\text{int}} - d_{\text{NaH}}^{as})\Theta[d_{\text{HH}}(R_{\text{HH}} - \Delta R_{\text{HH}})], \quad (\text{S7})$$

$$\Delta R_{\text{NaH}} = \Delta R_{\text{NaH}}^{as} + (\Delta R_{\text{NaH}}^{\text{int}} - \Delta R_{\text{NaH}}^{as})\Theta[d_{\text{HH}'}(R_{\text{HH}} - \Delta R_{\text{HH}})], \quad (\text{S8})$$

and

$$\Theta[x] = \frac{1}{2}(1 - \tanh[x]). \quad (\text{S9})$$

Singlet and triplet functions in Eqs. (S4) and (S5) are given by the following equations

$$S_{\text{HH},1} = (c_1 + c_2 R_{\text{HH}}) \exp[-c_3 R_{\text{HH}}] - R_{\text{HH}}^2 (c_4 + c_5 R_{\text{HH}}) \exp[-c_6 R_{\text{HH}}], \quad (\text{S10})$$

$$T_{\text{HH},1} = D_{\text{HH},1} X_{\text{HH},1} (X_{\text{HH},1} - 2), \quad (\text{S11})$$

$$X_{\text{HH},1} = \exp[-\beta_{\text{HH},1} (R_{\text{HH}} - R_{\text{HH},1}^0)], \quad (\text{S12})$$

$$S_{\text{MH},1} = S_{\text{MH},1}^{as} + (S_{\text{MH},1}^{int} - S_{\text{MH},1}^{as}) \gamma_1, \quad (\text{S13})$$

$$S_{\text{MH},1}^{as} = D_{\text{MH},1}^{as} X_{\text{MH},1}^{as} (X_{\text{MH},1}^{as} - 2), \quad (\text{S14})$$

$$X_{\text{MH},1}^{as} = \exp[-\beta_{\text{MH},1}^{as} (R_{\text{MH}} - R_{\text{MH},1}^{0,as})], \quad (\text{S15})$$

$$S_{\text{MH},1}^{int} = D_{\text{MH},1}^{int} X_{\text{MH},1}^{int} (X_{\text{MH},1}^{int} - 2), \quad (\text{S16})$$

$$X_{\text{MH},1}^{int} = \exp[-\beta_{\text{MH},1}^{int} (R_{\text{MH}} - R_{\text{MH},1}^{0,int})], \quad (\text{S17})$$

$$\begin{aligned} \gamma_1 = & \Theta[\alpha_{\text{MH},1} (R_{\text{MH}} - r_{\text{MH},1}^0)] \Theta[\alpha_{\text{MH},1} (R_{\text{MH}'} - r_{\text{MH},1}^0)] \\ & \times \Theta[-\alpha_{\text{HH},1} (R_{\text{HH}} - r_{\text{HH},1}^0)], \end{aligned} \quad (\text{S18})$$

$$T_{\text{MH},1} = t_1 \exp[-t_2 R_{\text{MH}}^6] + t_3 \exp[-t_4 R_{\text{MH}}], \quad (\text{S19})$$

$$S_{\text{HH},2} = T_{\text{HH},2} + (S_{\text{HH},2}^{as} - T_{\text{HH},2}) \Theta[(S_{\text{HH},2}^{as} - T_{\text{HH},2}) / c'], \quad (\text{S20})$$

$$S_{\text{HH},2}^{as} = S_{\text{HH},1} + \Delta E_3, \quad (\text{S21})$$

$$T_{\text{HH},2} = T_{\text{HH},2}^{as} + (T_{\text{HH},2}^{int} - T_{\text{HH},2}^{as}) \Theta[\alpha_{\text{MH},2} \{ \frac{1}{2} (R_{\text{MH}} + R_{\text{MH}'}) - r_{\text{MH},2} \}], \quad (\text{S22})$$

$$\alpha_{\text{MH},2} = \alpha_{\text{MH},2}^{90} + (\alpha_{\text{MH},2}^0 - \alpha_{\text{MH},2}^{90}) \cos^2(\chi), \quad (\text{S23})$$

$$r_{\text{MH},2} = r_{\text{MH},2}^{90} + (r_{\text{MH},2}^0 - r_{\text{MH},2}^{90}) \cos^2(\chi), \quad (\text{S24})$$

$$T_{\text{HH},2}^{as} = a_1 \exp[-a_2 R_{\text{HH}}] + (a_3 + a_4 R_{\text{HH}} + a_5 R_{\text{HH}}^2) \exp[-a_6 R_{\text{HH}}], \quad (\text{S25})$$

$$T_{\text{HH},2}^{int} = t_{\text{HH}}^{90} + (t_{\text{HH}}^0 - t_{\text{HH}}^{90}) \cos^2(\chi), \quad (\text{S26})$$

$$\begin{aligned} t_{\text{HH}}^{90} = & t_{\text{HH},1}^{90} \exp[-t_{\text{HH},2}^{90} R_{\text{HH}}] \\ & + (t_{\text{HH},3}^{90} + t_{\text{HH},4}^{90} R_{\text{HH}} + t_{\text{HH},5}^{90} R_{\text{HH}}^2 + t_{\text{HH},6}^{90} R_{\text{HH}}^3) \exp[-t_{\text{HH},7}^{90} R_{\text{HH}}], \end{aligned} \quad (\text{S27})$$

$$t_{\text{HH}}^0 = D_{\text{HH}}^0 X_{\text{HH}}^0 (X_{\text{HH}}^0 - 2), \quad (\text{S28})$$

$$X_{\text{HH}}^0 \exp[-\beta_{\text{HH}}^0 (R_{\text{HH}} - r_{\text{HH},0}^0)], \quad (\text{S29})$$

$$S_{\text{MH},2} = D_{\text{MH},2} \{ \exp[-\beta_{\text{MH},2}^{(1)} (R_{\text{MH}} - R_{\text{MH},2}^0) \\ - 2 \exp[-\beta_{\text{MH},2}^{(2)} (R_{\text{MH}} - R_{\text{MH},2}^0)] \} \quad (\text{S30})$$

$$T_{\text{MH},2} = t_{\text{MH}}^{90} + (t_{\text{MH}}^0 - t_{\text{MH}}^{90}) \cos^2(\chi), \quad (\text{S31})$$

$$t_{\text{MH}}^{90} = t_{\text{MH},1}^{90} \exp[-t_{\text{MH},2}^{90}] \\ + (t_{\text{MH},3}^{90} + t_{\text{MH},4}^{90} R_{\text{MH}} + t_{\text{MH},5}^{90} R_{\text{MH}}^2 + t_{\text{MH},6}^{90} R_{\text{MH}}^3) \exp[-t_{\text{MH},7}^{90} R_{\text{MH}}], \quad (\text{S32})$$

$$t_{\text{MH}}^0 = t_1^0 X_{\text{MH},2} (X_{\text{MH},2} - 2), \quad (\text{S33})$$

$$X_{\text{MH},2} \exp[-t_2^0 (R_{\text{MH}} - t_3^0)], \quad (\text{S34})$$

Parameters of the  $U_{11}$  and  $U_{22}$  functions are listed in Tables S-I and S-II, respectively.

The coupling function,  $U_{12}$ , is equal to

$$U_{12} = G \{F_{\text{MH}} + F_{\text{MH}'}\} \exp[-\eta(R_{\text{MH}} - R_{\text{MH}'})^2], \quad (\text{S35})$$

$$G = \left( \frac{R_{\text{MH}}^6 - R_{\text{MH}'}^6}{R_{\text{MH}}^6 + R_{\text{MH}'}^6} \right)^2 + \left\{ \left( \frac{R_{\text{MH}} - R_{\text{MH}'}}{R_{\text{HH}}} \right)^2 - \left( \frac{R_{\text{MH}}^6 - R_{\text{MH}'}^6}{R_{\text{MH}}^6 + R_{\text{MH}'}^6} \right)^2 \right\} \\ \times \Theta[-\lambda(R_0 - \sqrt{R_{\text{HH}}^2 + R_{\text{MH}}^2 + R_{\text{MH}'}^2})], \quad (\text{S36})$$

$$F_{\text{MH}} = A \exp[-\alpha(R_{\text{MH}} - R^0)^2], \quad (\text{S37})$$

$$\alpha = \beta + \frac{\gamma}{\varsigma + R_{\text{MH}}^3}, \quad (\text{S38})$$

$$A = A^c + (A^a - A^c) \Theta[-\alpha_A (R_{\text{HH}} - \rho_A^0)], \quad (\text{S39})$$

$$\beta = \beta^c + (\beta^a - \beta^c) \Theta[-\alpha_\beta (R_{\text{HH}} - \rho_\beta^0)], \quad (\text{S40})$$

$$\gamma = \gamma^c + (\gamma^a - \gamma^c) \Theta[-\alpha_\gamma (R_{\text{HH}} - \rho_\gamma^0)], \quad (\text{S41})$$

$$R^0 = R^{0c} + (R^{0a} - R^{0c}) \Theta[-\alpha_R (R_{\text{HH}} - \rho_R^0)]. \quad (\text{S42})$$

Parameters of the  $U_{12}$  function are listed in Table S-III.

**Table S-I.** Parameters of the  $U_{11}$  function

Parameter	Value	Parameter	Value
$D_e(\text{H}_2) / \text{eV}$	4.7469	$\beta_{\text{MH},1}^{as} / a_0^{-1}$	1.13054
$c_{1a} / \text{eV}$	1.5	$R_{\text{MH},1}^{0,as} / a_0$	3.34363
$c_{1b} / \text{eV}^{-1}$	1.0	$D_{\text{MH},1}^{int} / \text{eV}$	1.323042
$c_{1c} / a_0^{-1}$	0.225	$\beta_{\text{MH}}^{int} / a_0^{-1}$	0.81105
$c_1 / \text{eV}$	109.384	$R_{\text{MH},1}^{0,int} / a_0$	2.66667
$c_2 / \text{eV} a_0^{-1}$	463.033	$\alpha_{\text{MH},1} / a_0^{-1}$	1.05
$c_3 / a_0^{-1}$	6.240	$r_{\text{MH},1}^0 / a_0$	4.33333
$c_4 / \text{eV} a_0^{-2}$	13.654	$\alpha_{\text{HH},1} / a_0^{-1}$	1.65
$c_5 / \text{eV} a_0^{-3}$	20.717	$r_{\text{HH},1}^0 / a_0$	1.26667
$c_6 / a_0^{-1}$	2.032	$t_1 / \text{eV}$	6.279847
$D_{\text{HH},1} / \text{eV}$	0.02885656	$t_2 / a_0^{-6}$	0.0438425
$\beta_{\text{HH},1} / a_0^{-1}$	10.38036	$t_3 / \text{eV}$	5.546257
$R_{\text{HH},1}^0 / a_0$	1.237624	$t_4 / a_0^{-1}$	0.836095
$D_{\text{MH},1}^{as} / \text{eV}$	0.08		

**Table S-II.** Parameters of the  $U_{22}$  function

Parameter	Value	Parameter	Value
$\Delta E_1 / \text{eV}$	1.35	$t_{\text{HH},2}^{90} / a_0^{-1}$	4.47009
$\Delta E_2 / \text{eV}$	1.8	$t_{\text{HH},3}^{90} / \text{eV}$	4.48534
$d_{\text{MH}}^{\text{as}} / a_0^{-1}$	4.5	$t_{\text{HH},4}^{90} / \text{eV} a_0^{-1}$	-6.46276
$d_{\text{MH}}^{\text{int}} / a_0^{-1}$	2.9	$t_{\text{HH},5}^{90} / \text{eV} a_0^{-2}$	3.15396
$\Delta R_{\text{MH}}^{\text{as}} / a_0$	0.6	$t_{\text{HH},6}^{90} / \text{eV} a_0^{-3}$	-1.59912
$\Delta R_{\text{MH}}^{\text{int}} / a_0$	0.5	$t_{\text{HH},7}^{90} / a_0^{-1}$	1.77908
$d_{\text{HH}} / a_0^{-1}$	0.4	$D_{\text{HH}}^0 / \text{eV}$	0.8870172
$\Delta R_{\text{HH}} / a_0$	2.5	$\beta_{\text{HH}}^0 / a_0^{-1}$	0.8497374
$c_{2a} / \text{eV}$	0.8	$r_{\text{HH},0}^0 / a_0$	2.300265
$c_{2b} / \text{eV}^{-1}$	0.8	$D_{\text{MH},2} / \text{eV}$	1.4558
$c_{2c} / a_0^{-1}$	0.225	$\beta_{\text{MH},2}^{(1)} / a_0^{-1}$	3.135
$c' / \text{eV}$	0.8	$\beta_{\text{MH},2}^{(2)} / a_0^{-1}$	1.9
$\Delta E_3 / \text{eV}$	2.1037	$R_{\text{MH},2}^0 / a_0$	2.7
$\alpha_{\text{MH},2}^{90} / a_0^{-1}$	1.177425	$t_{\text{MH},1}^{90} / \text{eV}$	$2.205 \cdot 10^{-10}$
$\alpha_{\text{MH},2}^0 / a_0^{-1}$	0.921590	$t_{\text{MH},2}^{90} / a_0^{-1}$	15.2742
$r_{\text{MH},2}^{90} / a_0$	4.98436	$t_{\text{MH},3}^{90} / \text{eV}$	-2.87977
$r_{\text{MH},2}^0 / a_0$	6.004215	$t_{\text{MH},4}^{90} / \text{eV} a_0^{-1}$	81.95895
$a_1 / \text{eV}$	147.214	$t_{\text{MH},5}^{90} / \text{eV} a_0^{-2}$	-39.67522
$a_2 / a_0^{-1}$	3.915	$t_{\text{MH},6}^{90} / \text{eV} a_0^{-3}$	10.15369
$a_3 / a_0^{-1}$	41.275	$t_{\text{MH},7}^{90} / a_0^{-1}$	1.9545
$a_4 / \text{eV} a_0^{-1}$	10.505	$t_1^0 / \text{eV}$	0.24178
$a_5 / \text{eV} a_0^{-2}$	4.408	$t_2^0 / a_0^{-1}$	1.04404
$a_6 / a_0^{-1}$	2.032	$t_3^0 / a_0$	2.47204
$t_{\text{HH},1}^{90} / \text{eV}$	0.322400		

**Table S-III.** Parameters of the  $U_{12}$  function

Parameter	Value	Parameter	Value
$\eta / a_0^{-1}$	0.15	$\rho_\beta^0 / a_0$	0.895373
$\lambda / a_0^{-1}$	0.75	$\gamma^c / a_0$	2.0
$R_0 / a_0$	11.0	$\gamma^a / a_0$	11.683
$A^c / \text{eV}$	0.235737	$\alpha_\gamma / a_0^{-1}$	45.4595
$A^a / \text{eV}$	1.51495	$\rho_\gamma^0 / a_0$	-2.38193
$\alpha_A / a_0^{-1}$	0.502448	$R^{0c} / a_0$	2.33484
$\rho_A^0 / a_0$	4.05992	$R^{0a} / a_0$	2.62222
$\beta^c / a_0^{-2}$	230.065	$\alpha_R / a_0^{-1}$	20.4524
$\beta^a / a_0^{-2}$	0.071	$\rho_R^0 / a_0$	1.98942
$\alpha_\beta / a_0^{-1}$	0.469854		

## S.2. Contour plots

Contour plots of adiabatic and diabatic potential energy surfaces for the M–H–H' bond angle fixed at 90° are shown in Figures S-1 through S-5.

Fig. S-1.  $U_{11}$ . Contour values are 0.1, 0.2, 0.3, 0.4, 0.5, 0.6, 0.7, 0.8, 0.9, 1.1, 1.4, 1.8, 2.3, and 2.9 eV.

Fig. S-2.  $U_{22}$ . Contour values are 0.4, 0.5, 0.6, 0.7, 0.8, 0.9, 1.1, 1.4, 1.8, 2.3, and 2.9 eV.

Fig. S-3.  $U_{12}$ . Contour values are 0.02, 0.04, 0.06, 0.08, 0.10, 0.12, 0.14, 0.16, and 0.18 eV.

Fig. S-4.  $V_1$ . Contour values are 0.1, 0.2, 0.3, 0.4, 0.5, 0.6, 0.7, 0.9, 1.1, 1.4, 1.8, 2.3, and 2.9 eV.

Fig. S-5.  $V_2$ . Contour values are 0.4, 0.5, 0.6, 0.7, 0.8, 0.9, 1.1, 1.4, 1.8, 2.3, and 2.9 eV.

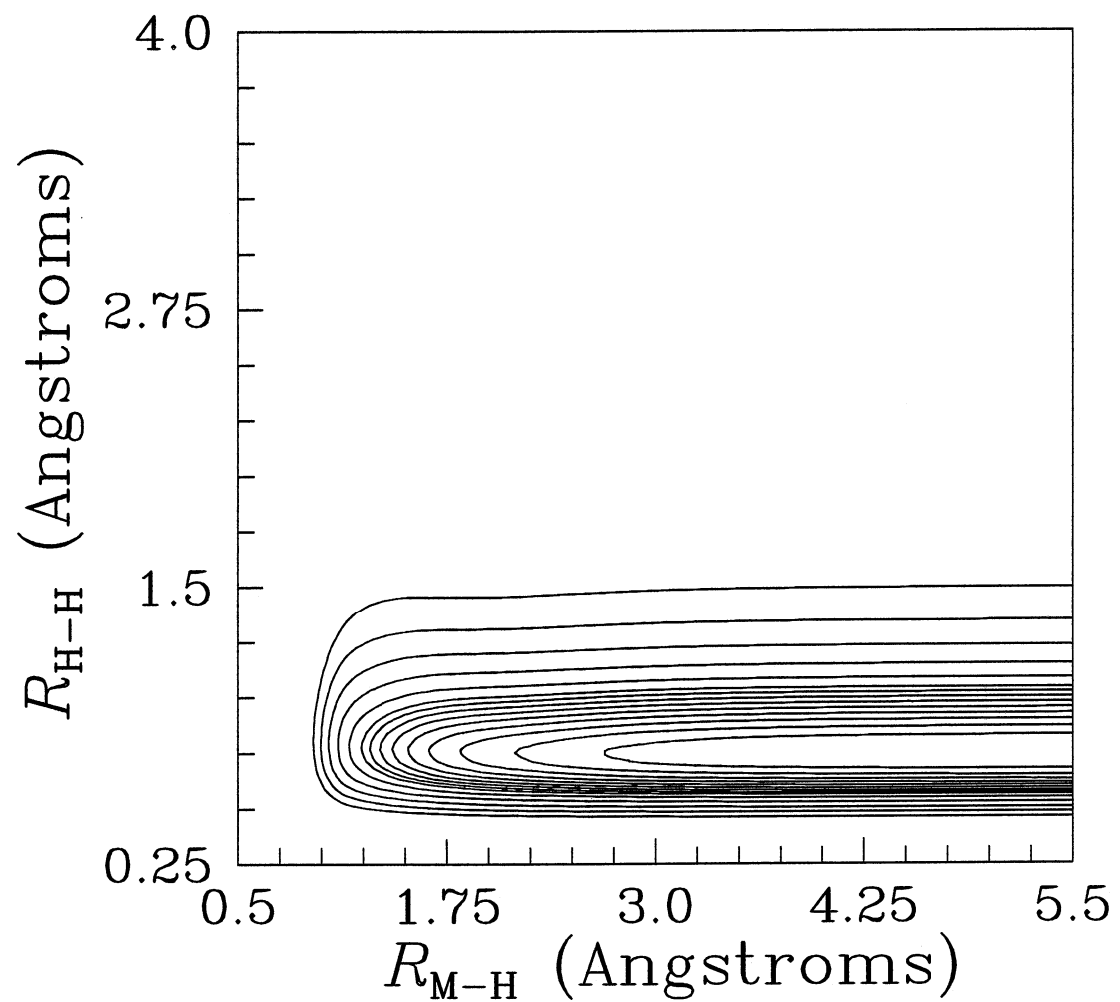


Fig. S-1

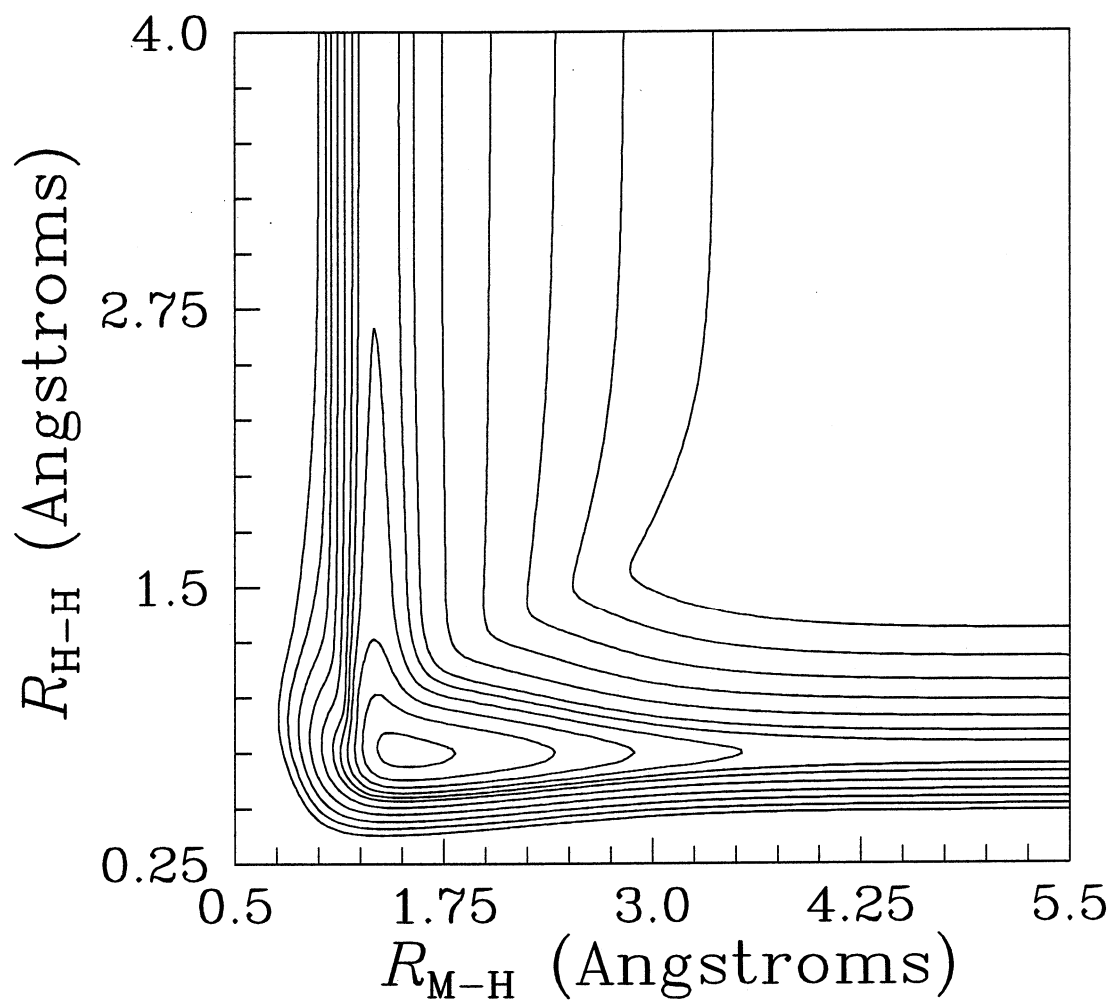


Fig. S-2

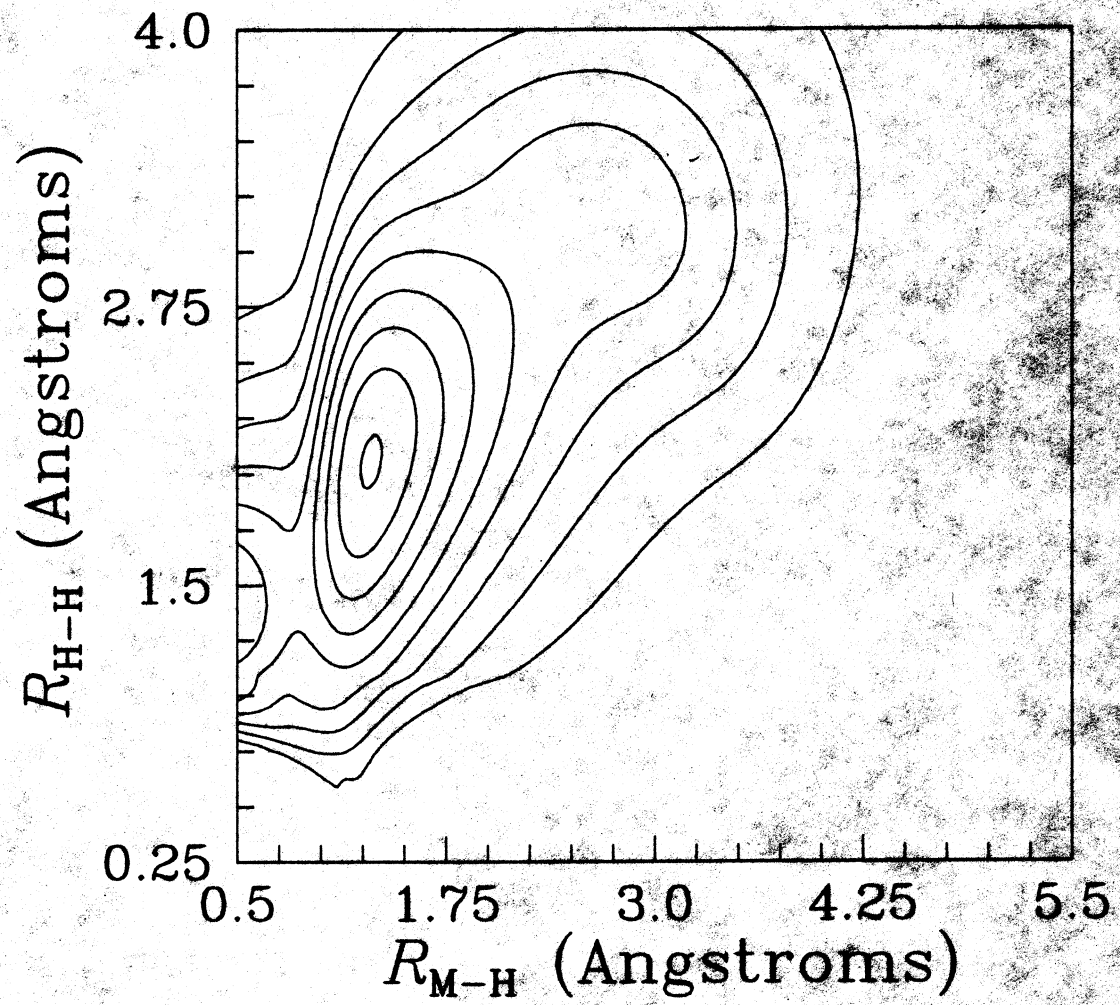


Fig. S-3

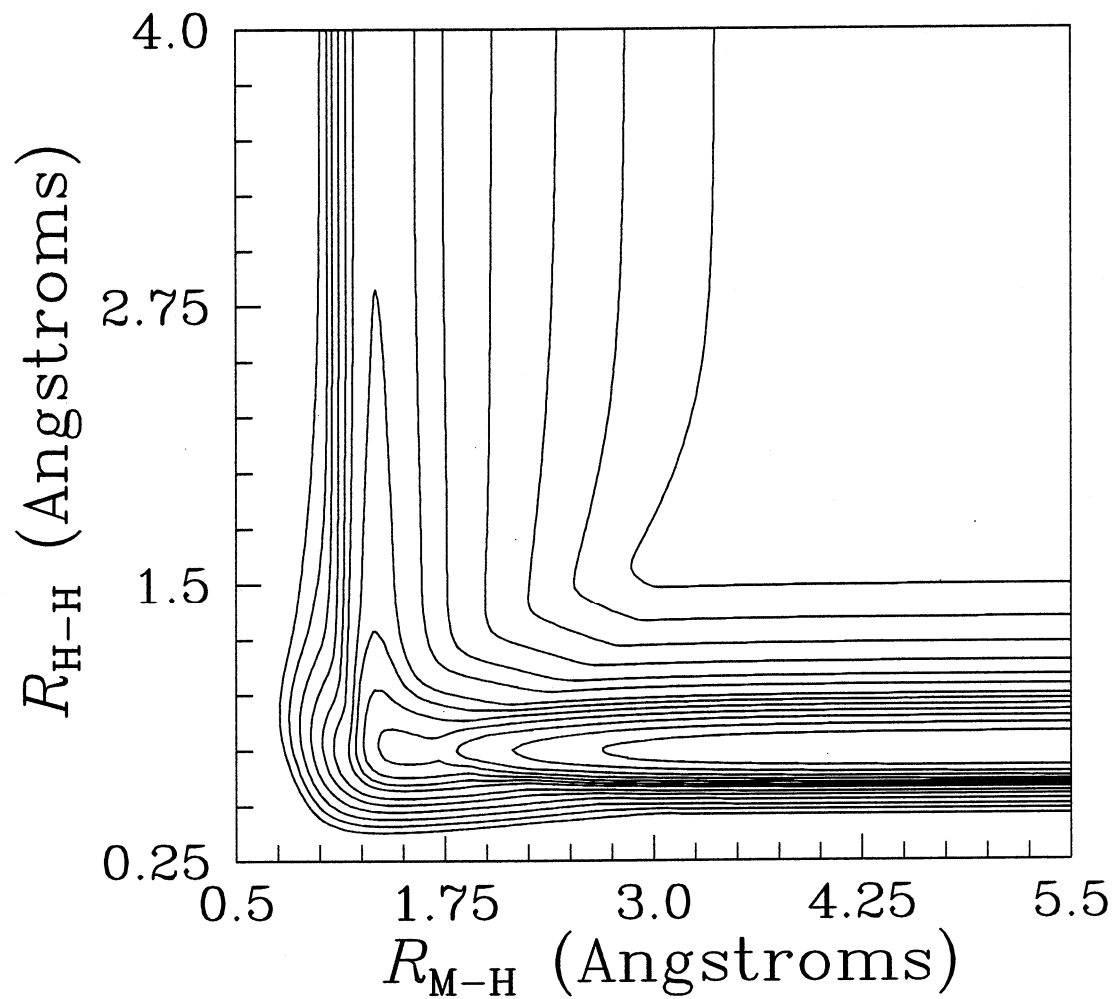


Fig. S-4

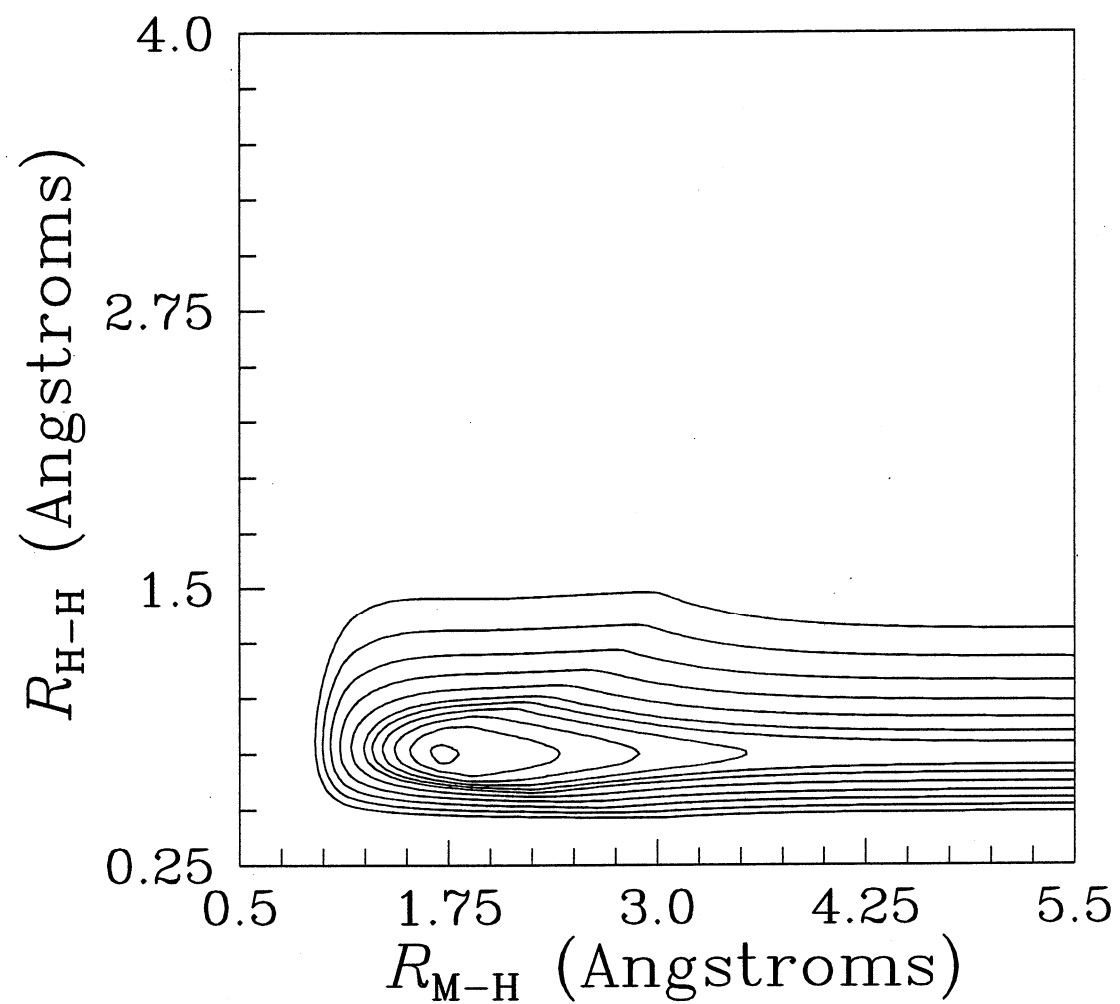


Fig. S-5

### S.3. Accurate quantal scattering calculations

Two sets of basis parameters used in the scattering calculations are given in Table S-IV. A description of the basis parameters used in Table S-IV is given in Table S-V. For further information on the basis set parameters the reader is directed elsewhere.<sup>1-3</sup>

Parameter set A was used for the results quoted in the paper. Parameter set B demonstrates the convergence of parameter set A with respect to the basis and numerical parameters. The state-to-state transition probabilities calculated using both of the basis sets are given in Table S-VI. The partially summed transition probabilities and moments of Tables II and III in the text are computed for all three basis sets in Table S-VII.

Vibrational and rotational states in the basis were selected using an energetic criterion,  $E_{\text{int,max}}$ . For all vibrational levels of the MH + H arrangement and the upper electronic state of the M + H<sub>2</sub> arrangement and for the lowest vibrational levels of the ground electronic state of the M + H<sub>2</sub> arrangement, all asymptotic states with vibrational and rotational energies less than or equal to  $E_{\text{int,max}}$  were included in the basis. The values listed in Table S-IV for  $j_{\text{max}}$  for these vibrational levels are consequences of the choices of  $E_{\text{int,max}}$ . Since we only calculate the even-symmetry (even, $j$ ) block of the scattering matrix, the value of  $j_{\text{max}}$  in the M + H<sub>2</sub> arrangement reflects the highest even- $j$  state for each  $v$ . Additional rotational states were used in the basis for the ground electronic state in the M + H<sub>2</sub> arrangement in the higher vibrational levels ( $v \geq 1$  for basis set A and  $v \geq 3$  for basis set B) to obtain convergence.

In order to assess the convergence of the basis set used in the production calculation, the state-to-state transition probabilities from sets A and B found in Table S-VI may be compared. This data shows that most of the state-selected transition probabilities of parameter set A are converged within 1% with respect to the results of parameter set B. Of the channels which are not converged within 1%, we find a maximum percentage difference of 1.7% for transition probabilities greater than  $2 \times 10^{-6}$  and a maximum percentage difference of 4.5% for transition probabilities less than  $2 \times 10^{-6}$ . The level of convergence of the state-to-state transition probabilities leads to excellent convergence, much better than 1%, of the partially summed transition probabilities and moments as may be seen in Table S-VII.

We note that the convergence of the present calculations is very tight, and it exceeds the level of convergence usually sought in quantum mechanical scattering calculations. We believe that such careful convergence checks are especially important when, as is the case here, one is reporting converged quantal results for a new class of problem since there are no results in the literature against which one can check the computer code. In addition to runs A and B for which results are shown in the tables, a large number of other calculations with a wide range of basis sets and numerical parameters gave very similar results for the quantities in Table S-VII and for most of the state-to-state transition probabilities.

The excellent convergence of the present calculations may be attributed in part to the use of coupled-channels Green's functions in the variational calculations; the efficacy of the approach has been demonstrated and discussed in previous work.<sup>4-12</sup>

## References

1. Schwenke, D. W.; Mielke, S. L.; and Truhlar, D. G., *Theor. Chim. Acta*, **1991**, *79*, 241.
2. Tawa, G. J.; Mielke, S. L.; Truhlar, D. G.; and Schwenke, D. W. In *Advances in Molecular Vibrations and Collision Dynamics*, Vol. 2B, Bowman, J. M.; Ed.; JAI Press: Greenwich, CT, 1994; pp. 45–116.
3. Tawa, G. J.; Mielke, S. L.; Truhlar, D. G.; and Schwenke, D. W. *J. Chem. Phys.* **1994**, *100*, 5751.
4. Staszewska, G.; Truhlar, D. G. *Chem. Phys. Lett.* **1986**, *130*, 341.
5. Staszewska, G.; Truhlar, D. G. *J. Chem. Phys.* **1987**, *86*, 2793.
6. Schwenke, D. W.; Haug, K.; Truhlar, D. G.; Sun, Y.; Zhang, J. Z. H.; Kouri, D. J. *J. Phys. Chem.* **1987**, *91*, 6080.
7. Schwenke, D. W.; Haug, K.; Zhao, M.; Truhlar, D. G.; Sun, Y.; Zhang, J. Z. H.; Kouri, D. J. *J. Phys. Chem.* **1988**, *92*, 3202.
8. Sun, Y.; Yu, C.-H.; Kouri, D. J.; Schwenke, D. W.; Halvick, P.; Mladenovic, M.; Truhlar, D. G.; *J. Chem. Phys.* **1989**, *91*, 1643.
9. Sun, Y.; Kouri, D. J.; Truhlar, D. G.; Schwenke, D. W. *Phys. Rev. A* **1990**, *41*, 4857.
10. Sun, Y.; Kouri, D. J.; Truhlar, D. G. *Nucl. Phys. A* **1990**, *508*, 41c.

11. Schwenke, D. W.; Mielke, S. L.; Truhlar, D. G.; *Theor. Chim. Acta* **1991**, *79*, 241.
12. Mielke, S. L.; Truhlar, D. G.; Schwenke, D. W. *J. Chem. Phys.* **1991**, *95*, 5097.

**Table S-IV.** OWVP basis set parameters for M + H<sub>2</sub> on the model surface at a total energy of 1.10 eV. Energies are given in eV and distances in unscaled bohrs. Set A was used for the results quoted in the paper, and Set B is used to demonstrate convergence. Neither basis A nor basis B contains a two-dimensional grid of gaussians; only channel functions are included in these two runs.

	Set A		Set B	
	M + H <sub>2</sub>	H + MH	M + H <sub>2</sub>	H + MH
<b>Basis Set Parameters</b>				
<i>vibrational-rotational basis</i>				
$E_{\text{int,max}}(\chi = 1)$	3.0 <sup>a</sup>	2.0	$D_e^{\text{a}}$	2.2
$j_{\max}(\chi = 1, \nu = 0)$	22	32	24	36
$j_{\max}(\chi = 1, \nu = 1)$	20	31	22	35
$j_{\max}(\chi = 1, \nu = 2)$	18	28	20	33
$j_{\max}(\chi = 1, \nu = 3)$	16	26	18	31
$j_{\max}(\chi = 1, \nu = 4)$	16	23	18	28
$j_{\max}(\chi = 1, \nu = 5)$	16	20	18	26
$j_{\max}(\chi = 1, \nu = 6)$	16	16	18	22
$j_{\max}(\chi = 1, \nu = 7)$	16	10	18	19
$j_{\max}(\chi = 1, \nu = 8)$	–	–	–	14
$j_{\max}(\chi = 1, \nu = 9)$	–	–	–	6
$E_{\text{int,max}}(\chi = 2)$	3.0	–	3.5	–
$j_{\max}(\chi = 2, \nu = 0)$	16	–	20	–
$j_{\max}(\chi = 2, \nu = 1)$	14	–	18	–
$j_{\max}(\chi = 2, \nu = 2)$	12	–	14	–
$j_{\max}(\chi = 2, \nu = 3)$	8	–	12	–
$j_{\max}(\chi = 2, \nu = 4)$	2	–	8	–
$j_{\max}(\chi = 2, \nu = 5)$	–	–	4	–
<i>translational basis</i>				
$S_1^G(\chi = 1)$	1.5	0.75	1.30	0.50
$S_u^G(\chi = 1)$	7.5	9.15	7.95	9.50
$m(\chi = 1)$	31	29	39	37
$\Delta^S(\chi = 1)$	0.2	0.3	0.175	0.25
$c(\chi = 1)$	0.64	1.0	0.56	0.81
$S_1^G(\chi = 2)$	1.5	–	1.25	–
$S_u^G(\chi = 2)$	7.5	–	8.00	–
$m^g, m^e(\chi = 2)$	21	–	28	–

$\Delta^S(\chi = 2)$	0.3	—	0.25	—
$c(\chi = 2)$	1.0	—	0.81	—

*open channels and basis functions*

$N^0$	12	22	12	22
$N^c$	97	172	118	238
$N$	109 <sup>b</sup>	194 <sup>b</sup>	130 <sup>c</sup>	260 <sup>c</sup>
$N_1^g$	10	22	10	22
$N_2^g$	2	—	2	—
$N_1^e$	68	172	76	238
$N_2^e$	29	—	42	—
$M_1^g$	310	638	390	814
$M_2^g$	42	—	56	—
$M_1^e$	2108	4988	2964	8806
$M_2^e$	609	—	1176	—
$M_1$	2418	5626	3354	9620
$M_2$	651	—	1232	—
$M$	3069 <sup>b</sup>	5626 <sup>b</sup>	4586 <sup>c</sup>	9620 <sup>c</sup>

*Numerical Parameters**screening parameters*

$\varepsilon_\chi$	$10^{-8}$	$10^{-10}$
$\varepsilon_{\text{rad}}$	$10^{-100}$	$10^{-120}$
$\varepsilon_t$	$10^{-8}$	$10^{-10}$
$\varepsilon_B$	$10^{-8}$	$10^{-10}$
$\varepsilon_W$	$10^{-8}$	$10^{-10}$

*FDBVM parameters*

$S_0^F$	1.0	1.0	0.5	0.5
$S_{N(F)+1}^F$	25.0	25.0	30.0	30.0
$N^{QS}$	120	80	150	100
$N^{QGL}$	10	7	12	9
$N^{FD}$	11	11	11	11
$N^{SD}$	40	40	50	50
$f^{SD}$	0.9	0.9	0.9	0.9
$N(F)$	1240	600	1850	950

*radial quadrature parameters*

$S_l^{\text{QR}}$	1.0	1.0	0.5	0.5
$S_u^{\text{QR}}$	15.0	15.0	20.0	20.0

*vibrational quadrature parameters*

$s_l^{\text{QV}}$	0.0	0.0	0.0	0.0
$s_u^{\text{QV}}$	6.0	6.0	7.0	7.0
$N^{\text{QV}}$	100	100	300	300
$N^{\text{QGLV}}$	1	1	2	2

*angular quadratures*

$N^{\text{QA}}$	100	100	150	150
$N_{12}^{\text{QA}}, N_{23}^{\text{QA}}$	100	100	150	150

*asymptotic quadratures*

$N(\text{HO})$	80	80	90	90
----------------	----	----	----	----

<sup>a</sup>For the M + H<sub>2</sub> arrangement on the ground-state surface, higher rotational states were included for the  $\nu \geq 1$  (set A) and  $\nu \geq 3$  (set B) vibrational levels in order to obtain converged results.  $D_e$  denotes the dissociation energy, 3.40 eV, for the H<sub>2</sub> diatomic molecule on the ground-state surface of the present set of model potential energy surfaces.

<sup>b</sup>Total number of channels and basis functions for parameter set A is 303 and 8695, respectively.

<sup>c</sup>Total number of channels and basis functions for parameter set B is 390 and 14206, respectively.

**Table S-V.** Description of basis set parameters for the OWVP scattering calculations.

$\chi$	electronic state index. $\chi = 1$ denotes the ground electronic state, and $\chi = 2$ denotes the first excited electronic state. Note that $\chi$ is also used to label the adiabatic potential energy surfaces.
$E_{\text{int,max}}$	maximum internal energy (relative to the overall zero of energy of the potential energy surfaces) up to which vibrational and rotational states were added to the basis.
$j_{\max}$	maximum rotational quantum number for a given electronic and vibrational state.
$S_1^G$	value of the unscaled coordinate $R$ at the center of the first (“lowest”) translational distributed Gaussian.
$S_u^G$	value of the unscaled coordinate $R$ at the center of the last (“uppermost”) translational distributed Gaussian.
$\Delta^S$	spacing in the unscaled coordinate $R$ of the translational distributed Gaussians.
$c$	overlap parameter of the translational distributed Gaussians.
$m^g, m^e$	number of basis functions per channel. In the present calculations, rotationally coupled Green’s functions are used in open channels and distributed gaussians times asymptotic eigenfunctions are used in closed channels.
$N^o$	number of open channels.
$N^c$	number of closed channels.
$N$	total number of channels.
$N_\chi^g$	number of channels on surface $\chi$ in which Green’s functions are used as basis functions.
$N_\chi^e$	number of channels on surface $\chi$ in which distributed gaussians times asymptotic eigenfunctions are used as basis functions.
$M_\chi^g$	total number of Green’s functions on surface $\chi$ in the basis.
$M_\chi^e$	total number of distributed gaussians times asymptotic eigenfunctions on surface $\chi$ in the basis.
$M_\chi$	total number of basis functions on surface $\chi$ .
$M$	total number of basis functions.
$\varepsilon_\chi$	exchange integral screening parameter.
$\varepsilon_{\text{rad}}$	radial integral screening parameter.
$\varepsilon_t$	translational basis screening parameter.
$\varepsilon_B$	screening parameter associated with the $W$ matrix.
$\varepsilon_W$	screening parameter associated with the $B$ matrix.

$S_0^F$	inner finite difference boundary condition point.
$S_{N(F)+1}^F$	outer finite difference boundary condition point.
$N^{QS}$	number of repetitions of Gauss-Legendre quadrature over the radial translational coordinate.
$N^{QGL}$	number of radial translational quadrature points per repetition of Gauss-Legendre quadrature.
$N^{FD}$	number of points used in the finite difference representation of the second derivative operator.
$N^{SD}$	number of additional points at the end of the finite difference grid where the step size decrease occurs.
$f^{SD}$	step size decrease factor.
$N(F)$	number of finite difference grid points.
$S_1^{QR}$	lower limit on the radial translational quadrature grid.
$S_u^{QR}$	upper limit on the radial translational quadrature grid.
$s_l^{QV}$	lower limit on the vibrational quadrature grid.
$s_u^{QV}$	upper limit on the vibrational quadrature grid.
$N^{QV}$	total number of quadrature points used in the Gauss-Legendre quadrature over the vibrational coordinate.
$N^{QGLV}$	number of quadrature points per repetition of Gauss-Legendre quadrature over the vibrational coordinate.
$N^{QA}$	number of points in the Gauss-Legendre quadrature used for the intra-arrangement angular integrals.
$N_{12}^{QA}, N_{23}^{QA}$	number of points in the Gauss-Legendre quadrature used for the inter-arrangement angular integrals.
$N(HO)$	number of functions in the harmonic oscillator basis used to expand the eigenvectors of the asymptotic vibrational-rotational diatomic potential.

**Table S-VI.** State-to-state transition probabilities for  $M + H_2$  on the model surface for parameter sets A and B. Initial and final states are labelled by  $|\alpha \chi v j\rangle$  where  $\alpha$  is the arrangement,  $\chi$  is the electronic quantum number, and  $v$  and  $j$  are the vibrational and rotational quantum numbers, respectively. Arrangement  $\alpha = 2$  is actually the symmetrized sum of the two  $MH + H$  arrangements.

Initial State	Final State	Set A	Set B
$ 1\ 2\ 0\ 0\rangle$	$ 1\ 1\ 0\ 0\rangle$	2.75(-4)	2.75(-4)
	$ 1\ 1\ 0\ 2\rangle$	4.06(-3)	4.07(-3)
	$ 1\ 1\ 0\ 4\rangle$	5.58(-3)	5.60(-3)
	$ 1\ 1\ 0\ 6\rangle$	2.18(-3)	2.19(-3)
	$ 1\ 1\ 0\ 8\rangle$	6.56(-3)	6.60(-3)
	$ 1\ 1\ 1\ 0\rangle$	1.62(-3)	1.62(-3)
	$ 1\ 1\ 1\ 2\rangle$	1.00(-2)	1.01(-2)
	$ 1\ 1\ 1\ 4\rangle$	3.68(-2)	3.70(-2)
	$ 1\ 1\ 0\ 10\rangle$	4.90(-8)	4.97(-8)
	$ 1\ 2\ 0\ 0\rangle$	1.01(-1)	9.99(-2)
	$ 1\ 1\ 1\ 6\rangle$	3.90(-7)	4.05(-7)
	$ 1\ 2\ 0\ 2\rangle$	2.93(-2)	2.94(-2)
	$ 2\ 2\ 0\ 0\rangle$	1.92(-2)	1.92(-2)
	$ 2\ 2\ 0\ 1\rangle$	8.39(-3)	8.44(-3)
	$ 2\ 2\ 0\ 2\rangle$	3.20(-2)	3.22(-2)
	$ 2\ 2\ 0\ 3\rangle$	6.14(-2)	6.14(-2)
	$ 2\ 2\ 0\ 4\rangle$	2.33(-2)	2.32(-2)
	$ 2\ 2\ 0\ 5\rangle$	1.34(-1)	1.34(-1)
	$ 2\ 2\ 0\ 6\rangle$	7.24(-2)	7.25(-2)
	$ 2\ 2\ 0\ 7\rangle$	3.06(-2)	3.07(-2)
	$ 2\ 2\ 0\ 8\rangle$	9.65(-2)	9.65(-2)
	$ 2\ 2\ 0\ 9\rangle$	1.85(-3)	1.83(-3)
	$ 2\ 2\ 0\ 10\rangle$	1.07(-2)	1.06(-2)
	$ 2\ 2\ 0\ 11\rangle$	2.50(-2)	2.50(-2)
	$ 2\ 2\ 0\ 12\rangle$	7.95(-4)	7.93(-4)
	$ 2\ 2\ 1\ 0\rangle$	3.43(-2)	3.43(-2)
	$ 2\ 2\ 1\ 1\rangle$	6.41(-2)	6.44(-2)
	$ 2\ 2\ 1\ 2\rangle$	5.08(-2)	5.09(-2)
	$ 2\ 2\ 0\ 13\rangle$	7.54(-3)	7.53(-3)
	$ 2\ 2\ 1\ 3\rangle$	6.84(-2)	6.86(-2)
	$ 2\ 2\ 1\ 4\rangle$	2.04(-2)	2.05(-2)
	$ 2\ 2\ 1\ 5\rangle$	1.58(-2)	1.58(-2)
	$ 2\ 2\ 0\ 14\rangle$	1.22(-7)	1.19(-7)
	$ 2\ 2\ 1\ 6\rangle$	2.46(-2)	2.47(-2)

$ 1\ 2\ 0\ 2\rangle$	$ 1\ 1\ 0\ 0\rangle$	3.07(-2)	3.07(-2)
	$ 1\ 1\ 0\ 2\rangle$	5.13(-2)	5.13(-2)
	$ 1\ 1\ 0\ 4\rangle$	2.52(-2)	2.51(-2)
	$ 1\ 1\ 0\ 6\rangle$	3.88(-3)	3.88(-3)
	$ 1\ 1\ 0\ 8\rangle$	2.55(-2)	2.54(-2)
	$ 1\ 1\ 1\ 0\rangle$	7.55(-3)	7.54(-3)
	$ 1\ 1\ 1\ 2\rangle$	9.38(-4)	9.26(-4)
	$ 1\ 1\ 1\ 4\rangle$	4.86(-2)	4.87(-2)
	$ 1\ 1\ 0\ 10\rangle$	2.02(-8)	2.00(-8)
	$ 1\ 2\ 0\ 0\rangle$	2.93(-2)	2.94(-2)
	$ 1\ 1\ 1\ 6\rangle$	1.41(-6)	1.47(-6)
	$ 1\ 2\ 0\ 2\rangle$	5.82(-2)	5.80(-2)
	$ 2\ 2\ 0\ 0\rangle$	2.00(-2)	2.00(-2)
	$ 2\ 2\ 0\ 1\rangle$	4.23(-2)	4.24(-2)
	$ 2\ 2\ 0\ 2\rangle$	3.57(-2)	3.56(-2)
	$ 2\ 2\ 0\ 3\rangle$	2.09(-2)	2.08(-2)
	$ 2\ 2\ 0\ 4\rangle$	3.41(-3)	3.47(-3)
	$ 2\ 2\ 0\ 5\rangle$	1.57(-2)	1.58(-2)
	$ 2\ 2\ 0\ 6\rangle$	5.55(-2)	5.56(-2)
	$ 2\ 2\ 0\ 7\rangle$	1.10(-1)	1.10(-1)
	$ 2\ 2\ 0\ 8\rangle$	5.59(-2)	5.58(-2)
	$ 2\ 2\ 0\ 9\rangle$	6.75(-2)	6.76(-2)
	$ 2\ 2\ 0\ 10\rangle$	8.05(-3)	8.02(-3)
	$ 2\ 2\ 0\ 11\rangle$	1.46(-2)	1.46(-2)
	$ 2\ 2\ 0\ 12\rangle$	2.47(-2)	2.46(-2)
	$ 2\ 2\ 1\ 0\rangle$	5.70(-3)	5.70(-3)
	$ 2\ 2\ 1\ 1\rangle$	5.05(-2)	5.05(-2)
	$ 2\ 2\ 1\ 2\rangle$	7.66(-2)	7.67(-2)
	$ 2\ 2\ 0\ 13\rangle$	1.09(-3)	1.10(-3)
	$ 2\ 2\ 1\ 3\rangle$	2.03(-2)	2.04(-2)
	$ 2\ 2\ 1\ 4\rangle$	6.43(-4)	6.36(-4)
	$ 2\ 2\ 1\ 5\rangle$	8.44(-2)	8.43(-2)
	$ 2\ 2\ 0\ 14\rangle$	2.76(-8)	2.73(-8)
	$ 2\ 2\ 1\ 6\rangle$	5.69(-3)	5.70(-3)

**Table S-VII.** Partially summed transition probabilities and moments (as computed in Tables II and III in the text) computed for parameter sets A and B of Table S-IV.

Initial State	Quantity	Set A	Set B
$ 1\ 2\ 0\ 0\rangle$	$P_{\text{quench}}$	0.0671	0.0674
	$P_{\text{react}}$	0.8023	0.8033
	$\langle v' \rangle$	0.3469	0.3475
	$\langle v'' \rangle$	0.7220	0.7220
	$\langle j' \rangle$	4.5209	4.5177
	$\langle j'' \rangle$	3.9231	3.9245
	$P(v' = 0)$	0.5240	0.5242
	$P(v' = 1)$	0.2784	0.2791
	$P(v'' = 0)$	0.0187	0.0187
	$P(v'' = 1)$	0.0485	0.0487
$ 1\ 2\ 0\ 2\rangle$	$P_{\text{quench}}$	0.1937	0.1936
	$P_{\text{react}}$	0.7188	0.7190
	$\langle v' \rangle$	0.3392	0.3392
	$\langle v'' \rangle$	0.2948	0.2951
	$\langle j' \rangle$	5.1449	5.1451
	$\langle j'' \rangle$	3.2357	3.2359
	$P(v' = 0)$	0.4749	0.4752
	$P(v' = 1)$	0.2438	0.2439
	$P(v'' = 0)$	0.1366	0.1364
	$P(v'' = 1)$	0.0571	0.0571